The Astrophysical Journal, 705:68–88, 2009 November 1 doi:10.1088/0004-637X/705/1/68

A *SPITZER* UNBIASED ULTRADEEP SPECTROSCOPIC SURVEY

B. Bertincourt[1,2], G. Helou[2], P. Appleton[2,3], P. Ogle[2], G. Lagache[1], T. Brooke[2], J-D. Smith[4], K. Sheth[2], D. Dale[5], M. Harwit[6], J-L. Puget[1], and H. Roussel[7]

[1] Institut d'Astrophysique Spatiale (IAS), Université Paris-Sud 11 and CNRS (UMR 8617), Bâtiment 121, F-91405 Orsay, France; benjamin.bertincourt@ias.u-psud.fr, guilaine.lagache@ias.u-psud.fr, jean-loup.puget@ias.u-psud.fr

[2] *Spitzer* Science Center, Infrared Processing and Analysis Center, California Institute of Technology, 1200 East California Boulevard, Pasadena, CA 91125, USA

[3] NASA *Herschel* Science Center, Infrared Processing and Analysis Center, California Institute of Technology, Pasadena, CA 91125, USA

[4] Steward Observatory, University of Arizona, Tucson, AZ, USA

[5] Department of Physics and Astronomy, University of Wyoming, Laramie, WY 82071, USA

[6] 511 H Street, SW, Washington DC 20024-2725, United States; Cornell University, Ithaca, NY, USA

[7] Institut d'Astrophysique de Paris, UPMC (Université Paris 6), 75014 Paris, France

Received 2009 January 6; accepted 2009 September 10; published 2009 October 7

ABSTRACT

We carried out an unbiased, spectroscopic survey using the low-resolution module of the infrared spectrograph (IRS) onboard *Spitzer* targeting two 2.6 square arcminute regions in the GOODS-North field. The IRS was used in a spectral mapping mode with 5 hr of effective integration time per pixel. One region was covered between 14 and 21 μm and the other between 20 and 35 μm. We extracted spectra for 45 sources. About 84% of the sources have reported detections by GOODS at 24 μm, with a median $f_\nu(24\ \mu\mathrm{m}) \sim 100\ \mu$Jy. All but one source are detected in all four IRAC bands, 3.6 to 8 μm. We use a new cross-correlation technique to measure redshifts and estimate IRS spectral types; this was successful for $\sim 60\%$ of the spectra. Fourteen sources show significant polycyclic aromatic hydrocarbon emission, four mostly SiO absorption, eight present mixed spectral signatures (low PAH and/or SiO) and two show a single line in emission. For the remaining 17, no spectral features were detected. Redshifts range from $z \sim 0.2$ to $z \sim 2.2$, with a median of 1. IR luminosities are roughly estimated from 24 μm flux densities, and have median values of $2.2 \times 10^{11} L_\odot$ and $7.5 \times 10^{11} L_\odot$ at $z \sim 1$ and $z \sim 2$, respectively. This sample has fewer active galactic nuclei than previous faint samples observed with the IRS, which we attribute to the fainter luminosities reached here.

Key words: galaxies: starburst – infrared: galaxies

Online-only material: color figures, extended figure

1. INTRODUCTION

The *Spitzer Space Telescope* (Werner et al. 2004) has multiplied by several orders of magnitude the volumes previously surveyed in the infrared for extragalactic objects (Soifer et al. 2008). Mid-infrared continuum surveys turned out to be especially fertile ground because of the superb sensitivity and speed of the 24 μm channel in the Multiband Imaging Photometer for *Spitzer* (MIPS) instrument (Rieke et al. 2004). These mid-infrared (MIR) surveys have established the dramatic evolution of galaxy populations over the last 10–12 billion years (e.g., Le Floc'h et al. 2004, 2005; Caputi et al. 2006; Papovich et al. 2007) previously *suggested* by *Infrared Space Observatory* (*ISO*) surveys (e.g., Elbaz et al. 1999; Oliver et al. 2000; Dole et al. 2001; Rowan-Robinson et al. 2004), and yielded rich samples of galaxies for follow-up. Critical to the interpretation of the data is the availability of multiple-band detections, which are used to constrain the redshifts, luminosities and sometimes the powering mechanism of sources. These constraints come about because the MIR spectra of galaxies are often strongly structured (Smith et al. 2007b; Armus et al. 2007), and sensitive to the presence of an active galactic nucleus (AGN), to optical depth, and to heating and dust geometry. By the same token, any single-band survey will have redshift-dependent biases resulting in a sampling of the population that varies with redshift. The obvious way to avoid this sampling bias is to survey in the dispersed light, a technique pioneered from the ground using objective-prism imaging in the visible.

In this paper, we report on a spectrally unbiased extragalactic census in the MIR using the Infrared Spectrograph (IRS) instrument (Houck et al. 2004) on *Spitzer*, and covering two spectral windows, 14–21 μm and 20–38 μm. Besides the specific results reported here, this survey illustrates the advantages of spectral mapping in the infrared. The placement of the windows allows us to attach an observed spectrum to the corresponding 24 μm source, and could therefore potentially address the bolometric correction for each source. The data also allow us to use spectral shapes, features and emission lines to characterize all detected sources, rather than only those sources selected for follow-up by the inevitably rough criteria of filtering on colors within the MIR or in combination with other bands (e.g., Yan et al. 2004; Weedman et al. 2006; Houck et al. 2007; Farrah et al. 2008). This unbiased examination of the emission line properties also yields a fair assessment of the distribution of line strengths and line-to-continuum ratios. Such an assessment constrains the frequency of line-dominated sources and might even yield examples of sources radiating largely line emission, and therefore very rarely picked up in broadband surveys. When our survey was proposed, a few examples of line-dominated sources in the MIR were known, including NGC 1569 (Lu et al. 2003). Today the most striking case known is probably the intergalactic shock in Stephan's Quintet, which emits more than 20% of its total infrared emission in the main three molecular hydrogen pure rotational transitions (Appleton et al. 2006). There is no reason to rule out scaled-up versions of these systems, which might be detectable with *Spitzer*.

Source confusion is often a limiting factor for infrared surveys, since the need to cool telescopes limits the size of the primary. The confusion limit appears in a variety of forms and definitions (Helou & Beichman 1990; Rowan-Robinson

2001; Lagache et al. 2003; Dole et al. 2004), but is ultimately dictated by the source density and its dependence on flux. A spectrally dispersed survey offers the spectral dimension as a discriminator among closely spaced sources, since the strongly featured shapes of MIR spectra would cause sources to peak almost always at different wavelengths. A method based on point-spread function (PSF) fitting at different wavelengths allows us to estimate accurately the confused sources positions at their peak wavelength as well as their contribution in flux to the neighboring sources. This spectral separation, solely relying on the knowledge of the PSF of the instrument, can be used as a prior to extract distinct spectra and thus disentangle sources, even if their broadband images overlap substantially.

This paper describes the survey design, observations, and data reduction in Section 2, describes the extraction of redshifts and spectral types from the data in Section 3, presents results on the distribution of redshifts and relation to broadband surveys in Section 4, and discusses those results in Section 5.

Throughout this paper, we assume a Λ-CDM cosmology with $H_0 = 70$ km s^{-1} Mpc^{-1}, $\Omega_M = 0.3$, and $\Omega_\Lambda = 0.7$.

2. OBSERVATIONS AND DATA REDUCTION

The goal was to carry out a blind survey rather than targeting specific sources. However, the general location of the surveyed area on the sky could be optimized to minimize sky brightness and improve access to ancillary data. We chose to place the survey in the Hubble Deep Field North (HDF-N) covered in the infrared by *Spitzer* as part of the GOODS survey (Dickinson et al. 2003). The availability of deep imaging with *Spitzer* allows us to relate the IRS data to continuum imaging immediately, and to avoid bright sources that would generate artifacts and reduce the effective size of the survey area. Additional ancillary data such as redshifts, ground-based photometry or high-resolution imaging all facilitate interpretation. We also made an effort to place the survey area in a particularly low-density region of GOODS-North (GOODS-N) judging by the 24 μm continuum map (Figure 1).

The GOODS 24 μm data are 84% complete around 80 μJy, and go as deep as 10 μJy, the weakest extractions reported by the GOODS team.

2.1. Observations

We observed a region in the HDF-N (Figure 1) with the Long-Low module of the IRS onboard *Spitzer*. Data are collected simultaneously from the two slits (LL1 and LL2) of the low-resolution module of the IRS, which cover different spectral ranges. We chose to maximize the depth of coverage with each slit, and therefore obtained two spatially and spectrally disjoint sets of data. The survey was executed using eight Astronomical Observation Requests (AORs) for a total of 46.5 hr of observation resulting in an integration time at full depth of 5 hr per sky position. Each AOR consists of 65 slit exposures following a 13 × 5 raster map with a step of one pixel (5.″1) between each exposure. Moreover, the eight AORs are dithered by 1/3 of a pixel in order to improve the PSF coverage at short wavelength. Those observations yield two adjacent areas, covering 14–21 μm (LL2) and 20–38 μm (LL1), respectively. Each field is covered to near-full depth over an area of 165″ × 56″ (innermost contour in Figure 1), corresponding to a number of spatial resolution elements of 33 × 11 for both LL1 and LL2. This is the most effective use of telescope time and instrument for an exploratory survey, rather than attempting to cover the same area with both submodules to get complete wavelength coverage.

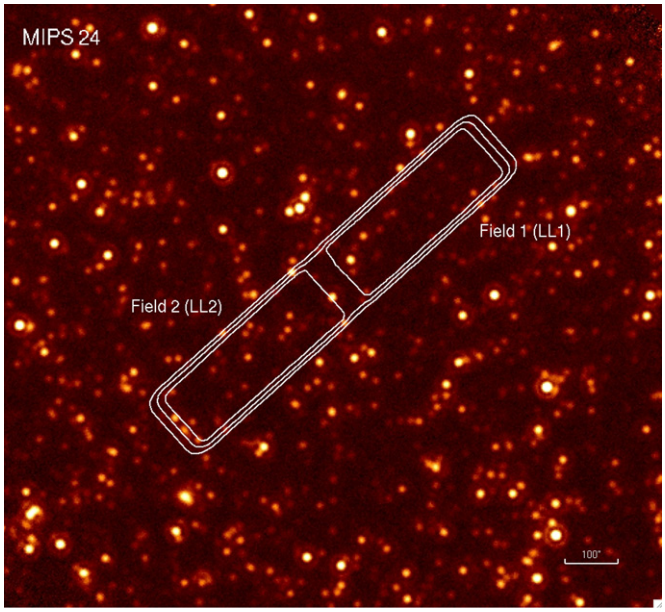

Figure 1. Depth of coverage of the *Spitzer* Unbiased Ultradeep Spectroscopic Survey overplotted on MIPS 24 μm observation (background) of the GOODS-N field (Dickinson et al. 2003). We show depth contours in white at values of 48, 95, and 143 (number of times a given position is covered by the IRS slit), respectively, from the innermost to the outermost contour.

(A color version of this figure is available in the online journal.)

2.2. Data Filtering and Cube Construction

Processing was pushed farther than the usual IRS pipeline products to obtain the best sensitivity. We applied additional reduction steps starting with the basic calibrated data (BCD) level processed through the version S15 of the pipeline. BCD are dispersed slit images that have been cleaned of radiation hit artifacts, rectified, and calibrated (see IRS data handbook: http://ssc.spitzer.caltech.edu/irs/dh/dh32.pdf).

First, we corrected for an upward drift in the BCD, manifested as a monotonic increase in the median signal with time for each set of consecutive AORs. This effect was assumed to be a detector effect, since the rise is too steep for any plausible phenomenon on the sky. It was thus removed as a function of time (robust polynomial fit). The robust fit was used to be resistant to a small number of outliers in the BCD offsets. The program used was *robust_poly_fit*, available as part of the IDL Astro Library. This procedure also removes any real time-invariant background, since we end up with a zero-median data set. The data at this point contain solely sources plus rogue signals. The latter originate in rogue pixels, whose dark current is abnormally high and varies with time and different sky brightness. Considering the impact of such artifacts on the faint sources we want to extract, a two-step removal was applied. The first step relies on sets of zero-median BCD taken close in time within an AOR, which we call an ensemble. After choosing the length of the zero-median ensemble, rogue pixels were subtracted by removing pixel-by-pixel a running robust trimmed linear fit to the ensemble from each BCD. The program used was *robust_linefit*, available as part of the IDL Astro Library. A robust linear fit rather than a robust mean was required to take into account some wavelength dependence in the drift described above. However, this residual drift was

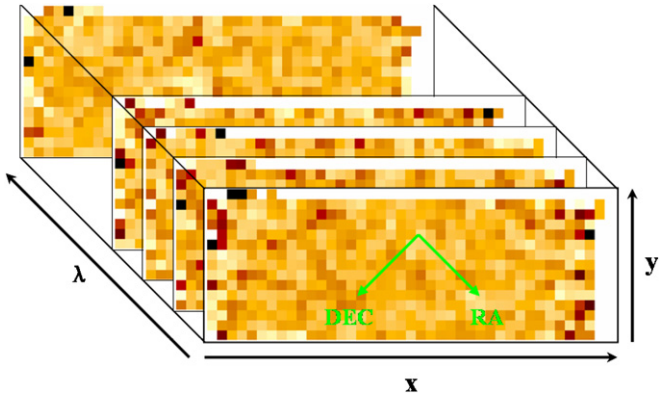

Figure 2. Representation of a reconstructed data cube using the CUBISM software developped by the SINGS team (Smith et al. 2007a).
(A color version of this figure is available in the online journal.)

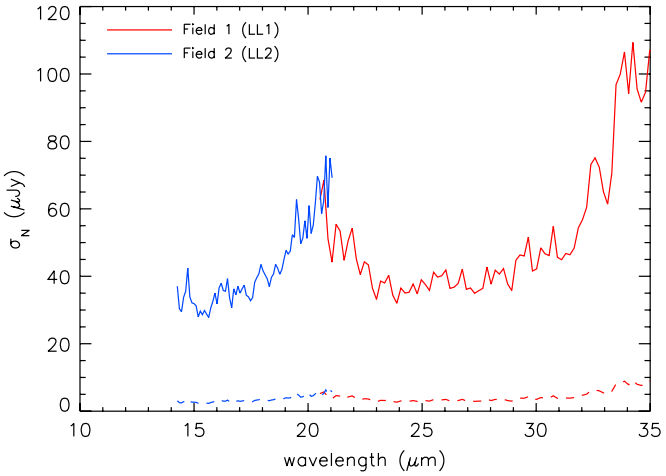

Figure 3. Standard deviation of the noise in our data set in each wavelength bin and for both fields (Field1 in red and Field 2 in blue). Solid lines illustrate the noise relative to each source extraction, whereas the dotted lines correspond to the noise in one single pixel of $(2\farcs55)^2$.
(A color version of this figure is available in the online journal.)

small, and the fits were close to robust means. This method only removes rogue signals thus ensuring that no correlated noise is added to the data. We used IRSCLEAN[8] after the ensemble subtraction to check how many additional bad pixels are found for ensembles of decreasing size. Changes in the number of bad pixels detected were found to be less than 2% when going below 1/4 of an AOR (32 frames) which was then chosen as the ensemble size. Additional rogue pixels were found and repaired at the single-BCD level using IRSCLEAN. IRSCLEAN fixes pixels by interpolating adjacent rows. One fixed iteration was done on each frame at a threshold of 4σ.

The second step removes the remaining rogue pixels in the map making. We used CUBISM developed by Smith et al. (2007a), a custom tool created for the assembly and analysis of spectral cubes from IRS spectral maps. Zero-median BCD frames were recombined into two spectral cubes providing two spatial and one spectral dimensions for each of LL1 (Field 1) and LL2 (Field 2). CUBISM uses trimmed averages over the set of individual measurements going into the signal for each pixel in the cube. The measurements are first weighted by the overlap fraction between BCD pixel area and cube pixel area, then averaged with trimming. We represent one of the cubes on a diagram in Figure 2. The considerable redundancy in the spatial coverage and the dithering between AORs oversample the sky sufficiently that the data cubes could be built with $(2\farcs55)^2$ pixels, oversampling by a factor of $\sim$2 the native spatial pixels. The cubes were not oversampled in the spectral dimension; thus, the sampling remains 0.092 μm pixel^{-1} in LL2 and ranges from 0.177 to 0.187 μm pixel^{-1} in LL1. The resulting cube dimensions are $79 \times 28 \times 95$ pixels covering $201'' \times 71'' \times 17.3$ μm for Field 1 and $79 \times 28 \times 75$ pixels covering $201'' \times 71'' \times 6.9$ μm for Field 2, corresponding to the outermost contours in Figure 1.

2.3. Characterization of the Noise

In order to estimate the noise in the data cubes and extract its variation with wavelength, we integrated each cube over its whole spectral range creating two-dimensional map-like planes (one per field). We applied an iterative sigma clipping on those maps to mask pixels containing sources, leaving about a thousand pixels in each field, excluding the edges where the noise increases dramatically due to decreasing coverage in the map. These remaining pixels are assumed to be dominated by noise. Spectra at all of these pixels were then used to compute the 1σ deviation of the noise at each wavelength. Note that due to the background subtraction, these spectra have a zero mean. Integrated over one oversampled $(2\farcs55)^2$ pixel, this standard deviation ranges between 2.7 μJy and 9.1 μJy in Field 1 (LL1, between 20 and 35 μm) and between 2.3 μJy and 6.3 μJy in Field 2 (LL2, between 14 and 21 μm; see dashed lines in Figure 3). The samples of positions used to extract the noise were then split into several spatially distinct subsets to check for any spatial dependency but no significant variation was found.

All information at $\lambda > 35$ μm in Field 1 (LL1) were discarded due to very high red-end noise. In the following, LL1 spectral range refers to a 20–35 μm band.

2.4. Source Detection and Extraction

The three-dimensional structure of the data was used to detect sources in both spectral and spatial dimensions. Sources were selected down to a low significance by scanning through X–λ planes by eye and then noting their positions in X–Y planes (summed over a portion of the spectral range) as can be seen in Figure 4. The signal was then estimated in the spatial vicinity of each position and summed over the spectral range where the source signal is higher than 2σ, using optimal extraction (Narron et al. 2007), applying a matched filter to the data. This estimated signal was then fitted by a two-dimensional Gaussian function in order to get the best positions and the best spectra for our sources. Finally, we estimate the integrated signal-to-noise ratio (S/N) for each optimally extracted spectrum over the full spectral range of LL1 or LL2 and keep only sources with integrated S/N greater than 2. We were able to extract 45 spectra, 20 in LL1 and 25 in LL2 (see Table 1 and Figures 5 and 6). We show in Figure 7 the S/Ns at peak achieved in our spectra. We also show the contracted bandwidth in μm over which our spectra achieve an S/N greater than 2. It should be noted that in estimating S/Ns, the noise values presented in the previous section need to be multiplied by a factor of 12 to account for the spatial integration implicit in optimal extraction (see solid lines in Figure 3).

[8] Software provided by the SSC, http://ssc.spitzer.caltech.edu/archanaly/contributed/irsclean/IRSCLEAN_MASK.html.

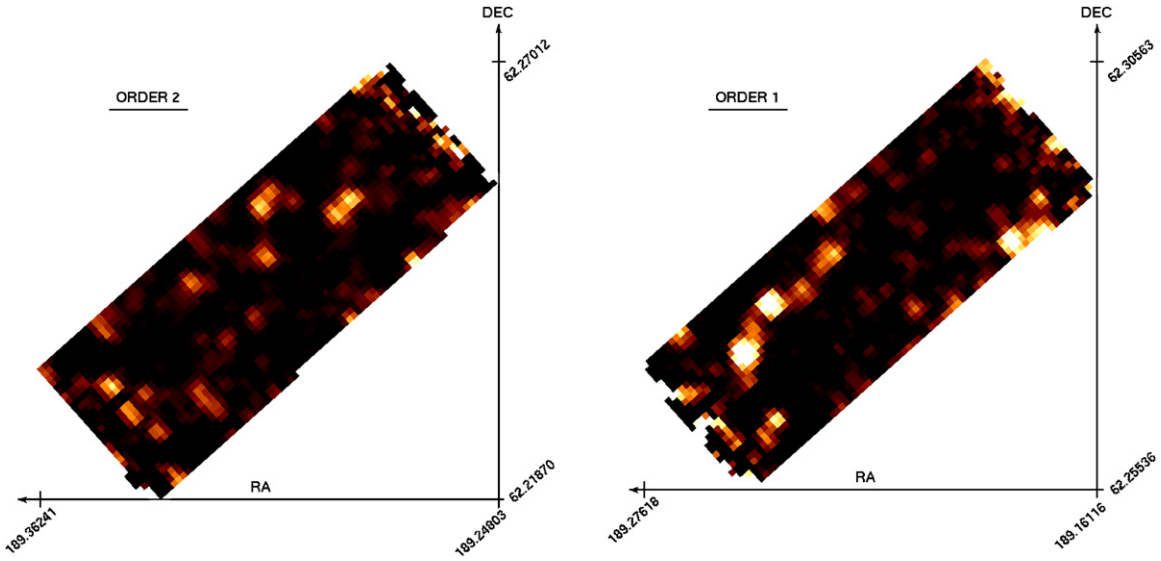

Figure 4. On the left, spatial map (*X*–*Y* plane, cf. Figure 2) of the Field 2 cube integrated over 14–19 μm. On the right, spatial map (*X*–*Y* plane) of the Field 1 cube integrated over 21–34 μm. Both maps are projected onto the sky.

(A color version of this figure is available in the online journal.)

2.5. Comparison with 24 μm GOODS Catalog

We correlated our sample with the MIPS 24 μm catalog from the GOODS survey Dickinson et al. (2003). Source detection in the MIPS image uses IRAC positions as priors, thus allowing us to select sources to a lower level than expected in the presence of confusion. The final MIPS catalog is described in more detail by Chary (2007); it has a 1σ depth of about 5 μJy and reaches a 84% completeness limit of 80 μJy. We select the nearest MIPS source up to 3 arcsec (corresponding to $\sim 2\sigma$ in IRS positioning accuracy) to be the counterpart of our IRS detections. We observe a mean difference of 1.″7 between IRS and MIPS counterpart coordinates. Results of the cross-identification (together with the IRAC catalog) are presented in Table 2. Considering both LL1 and LL2, 38 out of 45 sources (84%) of our sample have a 24 μm counterpart with a median $f_\nu(24\ \mu\mathrm{m})$ of 103 μJy. For LL1 only, the match rate is 90% (18 out of 20 sources). All MIPS sources with $S_{24} > 80$ μJy that fall into the region of near-full depth coverage of this survey are detected. The faintest MIPS counterpart to one of our extractions (SUUSS 18) has a 24 μm flux density of 47 μJy. This source is detected in LL1 with a maximum S/N of ~7 at 30.5 μm.

The 24 μm fluxes were used to check the flux calibration of our data set on sources extracted from Field 1 where the spectral range overlaps the MIPS 24 μm filter. We integrated the IRS LL1 spectra under the 24 μm bandpass. Sources with S/N greater than 2 in this integration were compared to their GOODS 24 μm flux counterpart in Figure 8. A linear regression on the data in Figure 8 yields

$$S_{24,\mathrm{IRS}} = 1.14\,(\pm 0.09) \times S_{24,\mathrm{MIPS}} - 27.1\,(\pm 16.2)\,.$$

As one might expect, the main source of error in estimating the 24 μm band fluxes using IRS spectra is the low S/N. We do not observe a clear bias or offset in the calibration.

In order to further compare our data to the photometric MIR data provided by the *GOODS* survey, we convolved the whole Field 1 cube by the MIPS 24 μm filter. Contours were extracted of the resulting IRS 24 μm map and overplotted on the released MIPS observation at the same wavelength (Figure 9). No bias or offset was observed in the comparison of source positions. We can detect a few examples of spatial confusion in the IRS map that are not present in the MIPS observation due to the better spatial resolution. These confused sources were however separated spectrally before extraction.

3. DETERMINING REDSHIFTS AND SPECTRAL TYPES FROM IRS SPECTRA

We have developed an original method to determine the redshift and spectral type of our sources using template spectra typical of various types of galaxies, and cross-correlation to fit the observed spectra to the templates. We describe here the method and present the results.

We selected a set of 21 template spectra: five templates dominated by aromatic feature emission presented in Smith et al. (2007b), 13 ULIRGs spectra from Armus et al. (2007), two radio galaxy and quasar spectra (P. Ogle 2007, private communication) and the spectrum of the Wolf–Rayet galaxy NGC1569 (Wu et al. 2006). For all these templates, we have full IRS low-resolution spectral coverage from 5 to 38 μm. All spectra were converted to rest frame before being used. They cover a full range of source properties from star-forming to AGN-dominated galaxies, and include the various known MIR signatures: aromatic features, silicate absorption, both high and low ionization lines, non-thermal continuum emission, and steeply rising thermal dust emission (see Figure 10 and Table 3).

3.1. Correlation Analysis of Individual Sources

The method is based on a two-parameter (redshift and spectral template) cross-correlation to estimate IRS spectroscopic redshift and determine a best-fit spectral type for our sources. For a given redshift z, we compute the Pearson product–moment correlation coefficient between data in the observed frame and each template spectrum, redshifted to z. The Pearson product is an estimate of the degree of linear relationship between two data vectors, usually noted $\rho_{S,T}$,

$$\rho_{S,T}(z) = \frac{\mathrm{Cov}(S,T)}{\sigma_S \cdot \sigma_T}, \qquad (1)$$

Table 1
Source Extraction Information

ID	Field	R.A.$_{IRS}$ (Degrees)	Decl.$_{IRS}$ (Degrees)	S/N[a]	Peak S/N[b] (μm)	Peak Wavelength[b] (μm)	$\Delta\lambda_{2\sigma}$[c] (μm)
SUUSS 1	LL1	189.176	62.2894	13.3	5.7	32.22	4.67
SUUSS 2	LL1	189.183	62.2848	45.9	10.2	31.67	11.43
SUUSS 3	LL1	189.187	62.2873	5.0	7.5	23.00	2.90
SUUSS 4	LL1	189.191	62.2835	7.7	4.7	31.67	3.54
SUUSS 5	LL1	189.198	62.2844	3.1	3.8	26.58	1.77
SUUSS 6	LL1	189.205	62.2947	2.2	1.5	31.67	0.16
SUUSS 7	LL1	189.208	62.2764	7.9	5.2	29.11	3.06
SUUSS 8	LL1	189.210	62.2827	5.3	6.2	31.85	3.38
SUUSS 9[d]	LL1	189.210	62.2869	1.2	3.2	33.50	0.16
SUUSS 10	LL1	189.217	62.2936	3.6	5.9	31.12	1.77
SUUSS 11	LL1	189.225	62.2907	11.5	8.7	22.65	5.64
SUUSS 12	LL1	189.229	62.2829	27.5	8.6	27.84	7.89
SUUSS 13	LL1	189.232	62.2822	3.8	7.1	24.43	4.19
SUUSS 14	LL1	189.237	62.2788	19.3	6.3	24.07	7.25
SUUSS 15	LL1	189.243	62.2638	22.6	6.2	33.50	7.73
SUUSS 16	LL1	189.244	62.2634	19.8	5.2	33.50	7.08
SUUSS 17	LL1	189.244	62.2771	67.6	15.4	33.32	12.56
SUUSS 18	LL1	189.246	62.2610	6.8	7.4	30.57	5.64
SUUSS 19	LL1	189.251	62.2687	21.4	8.1	31.85	8.21
SUUSS 20	LL1	189.251	62.2714	93.6	29.4	24.43	12.56
SUUSS 21	LL2	189.259	62.2532	14.3	6.6	15.28	3.08
SUUSS 22	LL2	189.263	62.2519	10.3	4.3	20.32	1.08
SUUSS 23	LL2	189.275	62.2552	6.2	3.9	15.92	1.08
SUUSS 24	LL2	189.283	62.2582	8.8	8.9	18.94	2.00
SUUSS 25	LL2	189.284	62.2539	37.6	10.4	15.83	4.75
SUUSS 26	LL2	189.288	62.2524	31.9	17.4	17.29	4.67
SUUSS 27	LL2	189.299	62.2538	11.0	5.5	16.56	2.58
SUUSS 28	LL2	189.305	62.2548	22.8	8.8	16.28	3.33
SUUSS 29	LL2	189.306	62.2472	32.3	16.4	14.91	3.92
SUUSS 30	LL2	189.307	62.2531	33.5	15.4	17.11	4.42
SUUSS 31	LL2	189.309	62.2403	14.5	7.2	19.95	2.83
SUUSS 32	LL2	189.315	62.2377	14.9	7.9	19.77	2.58
SUUSS 33	LL2	189.320	62.2292	15.9	7.8	18.03	3.00
SUUSS 34	LL2	189.320	62.2307	12.1	9.6	18.03	2.83
SUUSS 35	LL2	189.322	62.2478	4.8	6.2	15.00	1.67
SUUSS 36	LL2	189.324	62.2328	6.7	8.4	18.12	1.75
SUUSS 37	LL2	189.324	62.2439	32.5	12.3	15.83	4.75
SUUSS 38	LL2	189.330	62.2261	6.8	10.2	18.58	2.25
SUUSS 39	LL2	189.333	62.2269	24.5	14.9	16.65	2.50
SUUSS 40	LL2	189.334	62.2300	5.4	4.8	18.48	1.17
SUUSS 41	LL2	189.335	62.2313	11.3	5.7	15.18	2.58
SUUSS 42	LL2	189.340	62.2291	24.3	17.5	15.37	2.75
SUUSS 43	LL2	189.340	62.2415	6.9	5.8	18.12	1.67
SUUSS 44	LL2	189.345	62.2318	34.5	20.3	15.37	3.67
SUUSS 45	LL2	189.346	62.2385	21.7	11.4	15.09	3.50

Notes.
[a] S/N estimation when fluxes are integrated over the whole spectral range available (14–20 μm for LL2 and 20–35 μm for LL1).
[b] Maximum S/N achieved in each spectrum and the wavelength at which it peaks. The spectra were smoothed using a comprehensive Hanning window over three channels in order to avoid contribution from any potentially remaining hot pixel value.
[c] Contracted spectral bandwidth over which the spectra have flux densities higher than 2σ.
[d] SUUSS 9 is the [S IV] line source discussed in Section 4.3 which explains the low integrated S/N compared to its peak S/N.

where S and T are the data spectrum and the template spectrum, and σ_S and σ_T are the standard deviations of the source spectrum and the template spectrum in the wavelength range (LL1 or LL2), respectively. Note that σ_S is not the standard deviation of the noise presented in Section 2.3, but an estimate of the departure of each spectrum from a constant flux density (i.e., the usual definition of a standard deviation if we consider S as a random variable). Instead of a traditional cross-correlation with lag, we redshift the template by z, compute the Pearson product, $\rho_{S,T}(z)$, for that value of z as in Equation (1) above, and refer to it as the cross-correlation function. We build cross-correlation functions for $0 < z < 3$ with $\Delta z = 0.01$. Such functions vary between 1 (perfect linear correlation) and -1 (perfect linear anti-correlation). A cross-correlation maximum indicates a redshift identification with high likelihood, while the cross-correlation function's behavior away from the peak reflects the shape of the template in comparison to the observed spectrum.

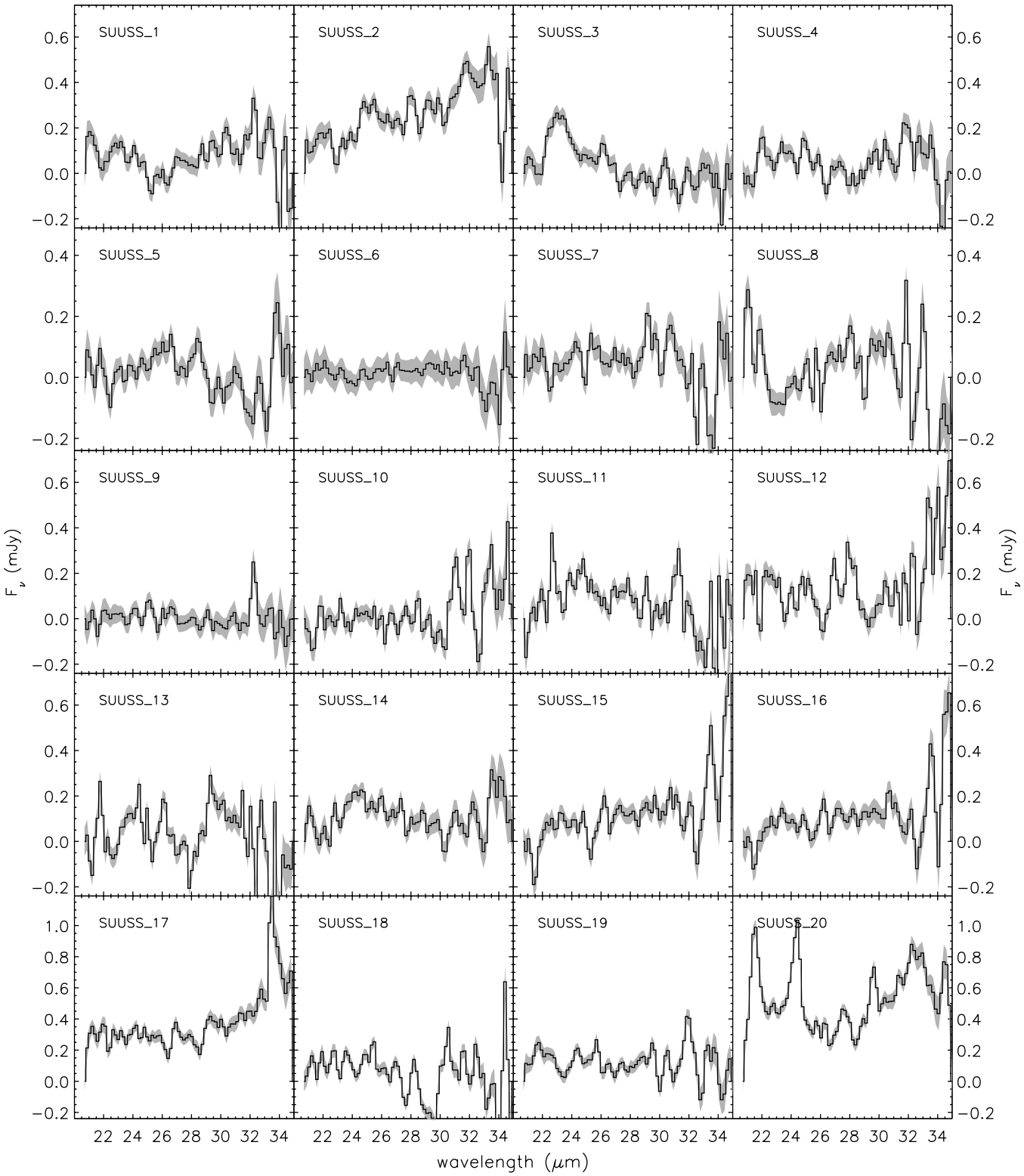

Figure 5. Spectra of the 18 sources extracted from FIELD 1. In shaded gray we plot the 1σ deviation for each spectrum. Two additional source spectra were extracted from this field. They are discussed in more details in Section 4.3.

3.2. Effect of Noise in the Spectra on Cross-correlation

The noise in the data has an important effect on the cross-correlation. Assuming that the templates are virtually noiseless in comparison to our spectra, the measured Pearson product–moment correlation coefficient is in fact

$$\tilde{\rho}_{S,T}(z) = \rho_{S,T}(z) \times \left(1 + \frac{\sigma_N^2}{\sigma_S^2}\right)^{-\frac{1}{2}}, \quad (2)$$

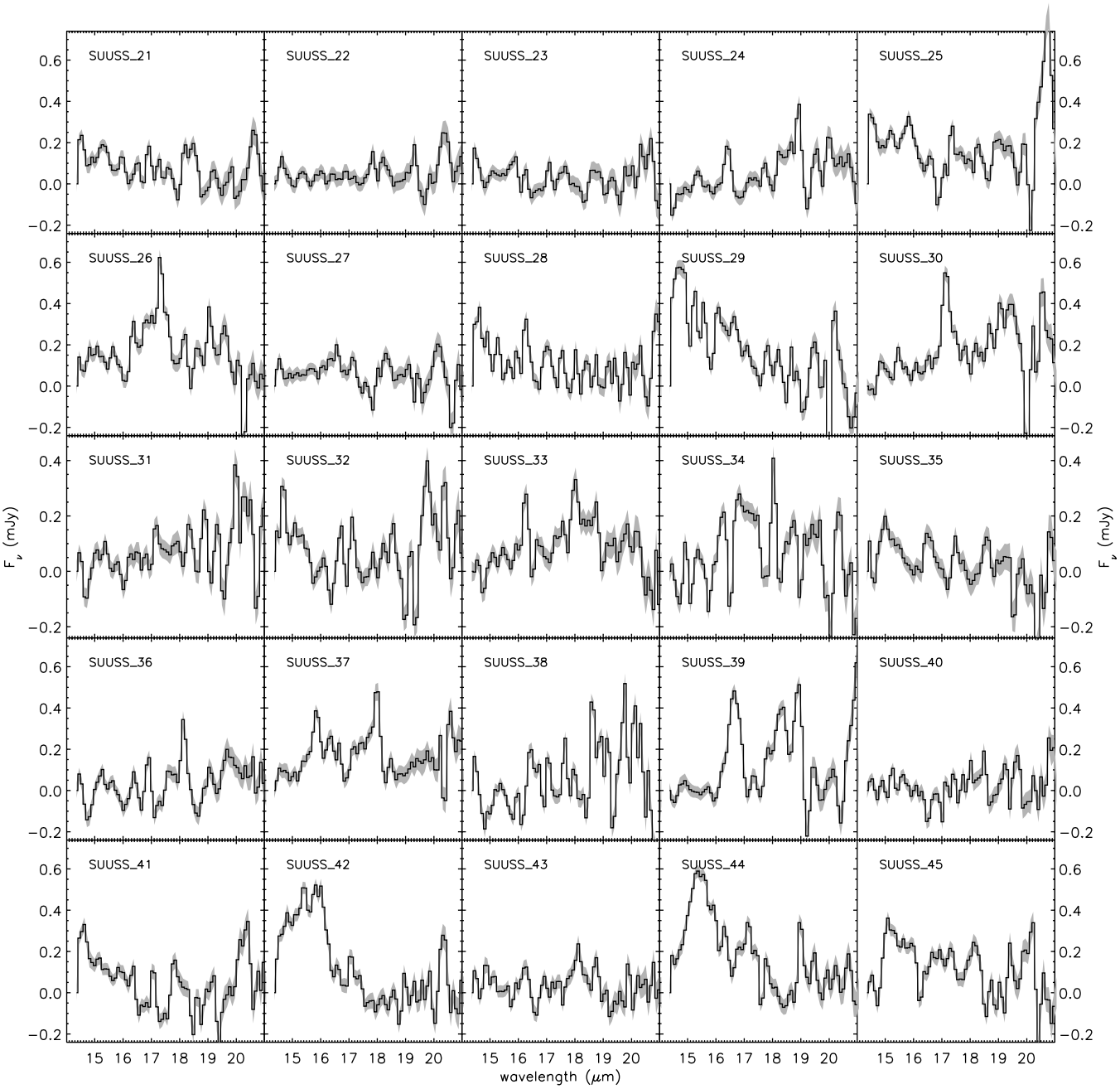

Figure 6. Spectra of the 25 sources extracted from FIELD 2. In shaded gray, we plot the 1σ deviation for each spectrum.

where σ_N is the standard deviation of the noise in our data set (see Figure 3). This equation shows that the noise will produce an overall decrease of the amplitude of the cross-correlation function. To quantify the effect of the noise on the cross-correlation function $\rho_{S,T}(z)$, we simulate data spectrum using the templates. The noise in our data has been characterized in Section 2.3, and its standard deviation, σ_N, extracted as a function of wavelength for both fields (LL1 and LL2) is shown in Figure 3. We define the S/N in our spectrum as

$$\mathrm{S/N} = \frac{\langle S \rangle_{\Delta\lambda\mathrm{max}}}{\langle \sigma_N \rangle_{\Delta\lambda\mathrm{max}}}, \quad (3)$$

where $\Delta\lambda$max is a small wavelength band around the maximum of the spectrum (2 μm and 1 μm in LL1 and LL2, respectively). We add noise in the template spectrum to reach a specific S/N then compute $\tilde{\rho}_{T(z),T}(z)$ (template with noise added versus template) which is equivalent to an auto-correlation function. We then extract the real value of the peak of the auto-correlation and plot it against the S/N in the spectrum (see Figure 11). At each given S/N, we make 30 realizations of the noise and average them to get the mean auto-correlation peak value. This relation, built on the template, is very helpful to estimate the S/N in our data from the value of the peak of the cross-correlation. As we can see from Equation (2), σ_S/σ_N controls the dynamic range of the cross-correlation function. That is equivalently a measure of the variability of the signal in the data spectrum.

3.3. Application to This Work: Breaking the Degeneracy

When working with low S/N spectra over a reduced wavelength range, the cross-correlation functions often contain

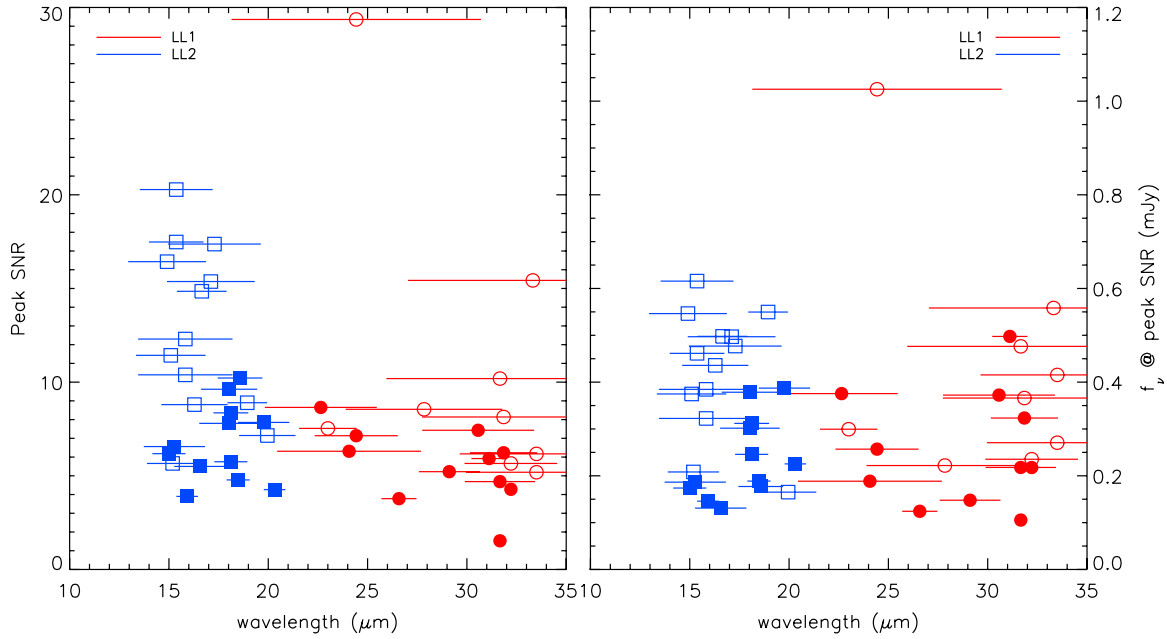

Figure 7. Left: maximum S/N achieved in each of our spectra versus the observed wavelength at which it peaks. Right: flux density f_ν of the SUUSS sources where their spectral S/Ns peak. In both plots, the bars in the wavelength direction relate to the contracted total spectral coverage over which each spectrum S/N is higher than 2. Empty symbols are sources for which MIPS $f_\nu(24\ \mu\mathrm{m}) > 100\ \mu$Jy, and filled symbols are sources for which MIPS $f_\nu(24\ \mu\mathrm{m}) < 100\ \mu$Jy as well as sources for which we do not have a MIPS 24 μm flux.

(A color version of this figure is available in the online journal.)

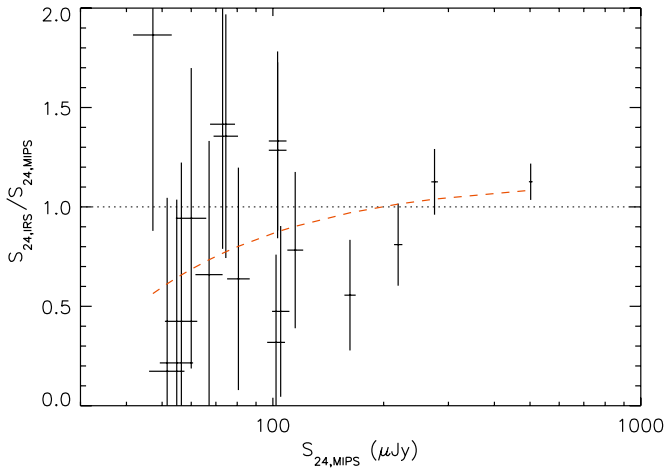

Figure 8. Ratio of IRS derived 24 μm and MIPS 24 μm fluxes against MIPS 24 μm flux for the SUUSS sources from Field 1 (which overlap MIPS 24 μm band). The dotted line is the one-to-one reference. The red dashed line is the linear fit between $S_{24,\mathrm{IRS}}$ and $S_{24,\mathrm{MIPS}}$ presented in Section 2.5.

(A color version of this figure is available in the online journal.)

several peaks at different redshifts of similar amplitude. Since the noise reduces the amplitude of the peaks of the cross-correlation by a factor directly linked to the S/N in the data spectrum, the value of the cross-correlation alone is not enough to decide between several candidate redshifts and candidate templates. The additional information we need to decide on the best match is provided by the shape of the cross-correlation function away from the peak. A given template is a good match for a given data spectrum if, under the same observational constrains (S/N and spectral coverage in this case), its "auto-correlation function" provides a good fit to the cross-correlation function *over the whole range of redshifts*.

Each maximum of the cross-correlation function yields a candidate solution consisting of a redshift–template combination. We use the template and redshift to simulate the observed spectrum and compute $\tilde{\rho}_{\tilde{T}(z_{\mathrm{max}}),T}(z)$, that we call an "auto-correlation function" as above:

$$\rho_{\tilde{T}(z_{\mathrm{max}}),T}(z) = \frac{\mathrm{Cov}(\tilde{T}(z_{\mathrm{max}}), T)}{\sigma_{\tilde{T}} \cdot \sigma_T}. \quad (4)$$

We use Figure 11 to pick the amount of noise to add to the template to reach the S/N corresponding to the cross-correlation amplitude of the candidate solution. The comparison between the cross-correlation and the "auto-correlation" tells us whether the choice of z and template recovers the shape of the correlation at lags other than zero, or equivalently redshifts other than the best-fit z. We compute the χ^2 between $\rho_{\tilde{T}(z\mathrm{max}),\mathrm{T}}(z)$ and $\tilde{\rho}_{S,T}(z)$ for each (z, T) candidate solution. The minimum χ^2, finally, gives us the best matching result which we call the IRS redshift z_{IRS}. We illustrate in Figure 12 the two-parameter nature of the fitting, which looks simultaneously for the best-fit redshift and best-fit template. This method was automatically applied to all extracted SUUSS spectra, without priors.

4. RESULTS

4.1. Redshift Distribution

The previous method is successful in determining the redshift for 28 sources (62% of the sample). For the remaining sources, the lack of redshift determination is mainly due to low S/N and/or the absence of any MIR feature in our spectral window. Results are presented in Table 4. We note that we have a comparable rate of successful redshift determination in Field 2 at 14–21 μm (17/25 sources or 68%) and in Field 1 at 20–35 μm (11/20 sources or 55%). We find a median redshift of 1.05 slightly larger than the median redshift of 0.935 found for the 24 μm flux-limited sample ($S_{24} > 80\ \mu$Jy) by Caputi et al. (2007). Interestingly, mean redshifts for each field are quite

Table 2
Spitzer Multi-wavelength Data

Name	R.A.$_{IRS}$ (Degrees)	Decl.$_{IRS}$ (Degrees)	$S_{3.6}$[a] (μJy)	$S_{4.5}$[a] (μJy)	$S_{5.8}$[a] (μJy)	S_{8}[a] (μJy)	S_{24}[b] (μJy)
SUUSS 1	189.176	62.2894	33.60 ± 0.04	38.60 ± 0.05	34.40 ± 0.30	23.60 ± 0.32	115.0 ± 5.5
SUUSS 2	189.183	62.2848	31.00 ± 0.04	24.70 ± 0.05	22.70 ± 0.30	41.20 ± 0.32	219.0 ± 5.9
SUUSS 3	189.187	62.2873	12.00 ± 0.03	13.40 ± 0.05	14.80 ± 0.30	10.10 ± 0.32	162.0 ± 4.2
SUUSS 4	189.191	62.2835	29.30 ± 0.04	22.70 ± 0.05	18.20 ± 0.30	14.90 ± 0.32	80.6 ± 4.5
SUUSS 5	189.198	62.2844	5.10 ± 0.03	6.35 ± 0.05	8.32 ± 0.30	6.37 ± 0.32	56.4 ± 4.9
SUUSS 6	189.205	62.2947	5.13 ± 0.03	5.66 ± 0.05	6.49 ± 0.33	6.00 ± 0.35	54.8 ± 5.4
SUUSS 7	189.208	62.2764	18.30 ± 0.03	14.90 ± 0.05	11.80 ± 0.30	20.50 ± 0.33	60.0 ± 5.9
SUUSS 8	189.210	62.2827	10.60 ± 0.03	10.80 ± 0.05	8.64 ± 0.31	7.68 ± 0.33	51.6 ± 6.8
SUUSS 9	189.210	62.2869	...	...	...	...	...
SUUSS 10	189.217	62.2936	3.56 ± 0.03	2.14 ± 0.05	0.92 ± 0.34	0.54 ± 0.36	...
SUUSS 11	189.225	62.2907	7.68 ± 0.03	8.02 ± 0.05	7.20 ± 0.34	6.16 ± 0.37	73.0 ± 5.8
SUUSS 12	189.229	62.2829	45.70 ± 0.04	34.80 ± 0.06	28.80 ± 0.33	34.10 ± 0.36	103.0 ± 5.7
SUUSS 13	189.232	62.2822	16.70 ± 0.04	13.00 ± 0.05	11.60 ± 0.33	9.09 ± 0.36	67.1 ± 5.0
SUUSS 14	189.237	62.2788	6.84 ± 0.03	7.72 ± 0.05	9.91 ± 0.33	6.69 ± 0.35	74.5 ± 5.7
SUUSS 15	189.243	62.2638	12.10 ± 0.03	10.70 ± 0.05	7.69 ± 0.30	13.90 ± 0.32	102.0 ± 5.5
SUUSS 16	189.244	62.2634	12.10 ± 0.03	10.70 ± 0.05	7.69 ± 0.30	13.90 ± 0.32	105.0 ± 6.1
SUUSS 17	189.244	62.2771	66.70 ± 0.05	60.20 ± 0.06	41.70 ± 0.34	120.00 ± 0.37	275.0 ± 5.7
SUUSS 18	189.246	62.2610	13.20 ± 0.03	13.20 ± 0.05	11.60 ± 0.29	7.69 ± 0.32	47.2 ± 6.3
SUUSS 19	189.251	62.2687	15.70 ± 0.03	11.30 ± 0.05	8.33 ± 0.32	8.69 ± 0.34	103.0 ± 8.5
SUUSS 20	189.251	62.2714	36.60 ± 0.04	27.20 ± 0.06	29.90 ± 0.33	26.50 ± 0.35	502.0 ± 7.7
SUUSS 21	189.259	62.2532	15.50 ± 0.03	10.60 ± 0.05	8.76 ± 0.29	7.55 ± 0.31	71.0 ± 6.2
SUUSS 22	189.263	62.2519	6.58 ± 0.03	5.94 ± 0.05	2.66 ± 0.29	3.52 ± 0.31	...
SUUSS 23	189.275	62.2552	13.20 ± 0.03	9.33 ± 0.05	9.37 ± 0.31	7.66 ± 0.33	59.2 ± 6.3
SUUSS 24	189.283	62.2582	8.79 ± 0.03	11.50 ± 0.05	14.30 ± 0.32	10.70 ± 0.36	219.0 ± 6.5
SUUSS 25	189.284	62.2539	27.40 ± 0.04	18.80 ± 0.05	20.10 ± 0.32	14.80 ± 0.35	198.0 ± 5.9
SUUSS 26	189.288	62.2524	26.40 ± 0.04	24.50 ± 0.06	18.50 ± 0.32	17.90 ± 0.35	123.0 ± 5.4
SUUSS 27	189.299	62.2538	21.50 ± 0.04	18.70 ± 0.06	13.30 ± 0.34	29.90 ± 0.38	88.1 ± 6.2
SUUSS 28	189.305	62.2548	16.50 ± 0.04	12.00 ± 0.06	12.30 ± 0.35	9.93 ± 0.41	169.0 ± 6.3
SUUSS 29	189.306	62.2472	74.10 ± 0.05	54.80 ± 0.06	46.30 ± 0.34	33.00 ± 0.38	241.0 ± 7.0
SUUSS 30	189.307	62.2531	34.70 ± 0.04	27.70 ± 0.06	26.30 ± 0.35	32.80 ± 0.41	149.0 ± 6.2
SUUSS 31	189.309	62.2403	31.50 ± 0.04	25.40 ± 0.06	21.70 ± 0.33	21.80 ± 0.36	103.0 ± 6.2
SUUSS 32	189.315	62.2377	16.30 ± 0.04	11.00 ± 0.06	12.20 ± 0.33	7.94 ± 0.37	76.6 ± 6.5
SUUSS 33	189.320	62.2292	2.32 ± 0.03	1.68 ± 0.05	1.34 ± 0.31	0.66 ± 0.35	...
SUUSS 34	189.320	62.2307	18.00 ± 0.04	15.60 ± 0.05	11.10 ± 0.32	12.60 ± 0.36	66.0 ± 5.3
SUUSS 35	189.322	62.2478	10.20 ± 0.04	7.19 ± 0.06	7.06 ± 0.36	5.71 ± 0.42	81.1 ± 6.4
SUUSS 36	189.324	62.2328	14.20 ± 0.04	11.90 ± 0.06	8.11 ± 0.33	16.70 ± 0.37	54.5 ± 5.6
SUUSS 37	189.324	62.2439	22.50 ± 0.04	20.80 ± 0.06	15.50 ± 0.36	38.50 ± 0.42	119.0 ± 6.7
SUUSS 38	189.330	62.2261	1.33 ± 0.03	1.38 ± 0.05	0.833 ± 0.31	1.87 ± 0.36	...
SUUSS 39	189.333	62.2269	77.90 ± 0.05	61.30 ± 0.06	50.60 ± 0.33	63.80 ± 0.37	185.0 ± 4.6
SUUSS 40	189.334	62.2300	35.50 ± 0.04	25.50 ± 0.06	23.00 ± 0.34	17.30 ± 0.39	...
SUUSS 41	189.335	62.2313	35.50 ± 0.04	25.50 ± 0.06	23.00 ± 0.34	17.30 ± 0.39	142.0 ± 5.6
SUUSS 42	189.340	62.2291	43.50 ± 0.05	34.90 ± 0.06	26.70 ± 0.34	25.60 ± 0.39	217.0 ± 6.4
SUUSS 43	189.340	62.2415	6.52 ± 0.04	5.31 ± 0.06	4.34 ± 0.38	3.01 ± 0.43	...
SUUSS 44	189.345	62.2318	2.60 ± 0.04	1.79 ± 0.06	1.17 ± 0.35	1.66 ± 0.42	301.0 ± 4.7
SUUSS 45	189.346	62.2385	32.60 ± 0.04	24.90 ± 0.07	19.20 ± 0.38	16.80 ± 0.43	148.0 ± 5.8

Notes.
[a] IRAC photometry from GOODS legacy program, Dickinson et al. (2003).
[b] MIPS 24 μm photometry from GOODS-N, Chary (2007).

different and are equal to 1.25 and 0.92 in Field 1 (LL1) and Field 2 (LL2), respectively. We identify more higher redshift sources in Field 1 (4/20 sources with $z > 2$) than in Field 2 (1/25 sources with $z > 2$) which is probably due to the different rest-frame wavelength ranges observed by LL1 (6.7 to 11.3 μm at $z = 2$) and LL2 (4.7–6.7 μm at $z = 2$). The most distant galaxy is at $z \sim 2.2$.

We compare the IRS spectroscopic redshift of our sample with the optical spectroscopic redshifts from Wirth et al. (2004; 13 sources, see Table 4 and Figure 13). The mean of $\Delta z/(1+z)$ is equal to 4.3×10^{-3}, and its standard deviation is of 1.0×10^{-2}. This shows that, even with very noisy IRS spectra, our method is able to determine MIR spectroscopic redshifts as accurate as 1% of $(1 + z)$. Where an optical spectroscopic redshift is not available, and the MIPS flux density is higher than 83 μJy, we use photometric redshift from Caputi et al. (2007). The seven such sources in our sample yield a $< \Delta z/(1+z) >$ of 1.5×10^{-2} with a standard deviation of 6.6×10^{-2}. This dispersion is higher than expected from the photometric redshift characterization in Caputi et al. (2007).

Of the 17 sources without an IRS redshift, five have an optical spectroscopic redshift and 12 have no redshift at all. As stated in Section 2.5, we do detect all sources with MIPS $S_{24} > 80$ μJy in our sample thus reaching comparable depth as the sample used

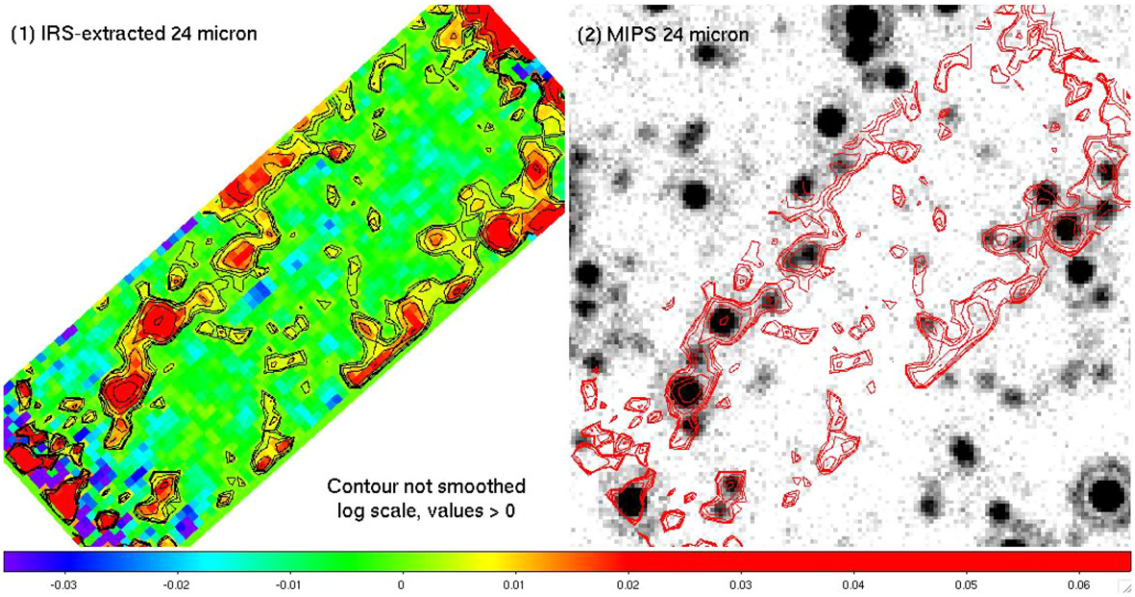

Figure 9. Left: an IRS-computed 24 μm map for Field 1. The contour levels were computed in logarithmic scale in order to highlight faint sources. The first contours correspond to 0.3σ. Right: the contours extracted from the left panel are overplotted on the GOODS-N MIPS 24 μm observations (Dickinson et al. 2003).

Table 3
Templates IR Properties

Template	z	6.2 μm EQW (μm)	7.7 μm EQW (μm)	$\log(L_{\rm IR}[L_\odot])$	Ref.
Mrk231	0.042	0.011	...	12.57	1
Mrk273	0.038	0.171	...	12.15	1
Mrk463	0.051	...	0.029	11.70	2
Mrk1014	0.163	0.048	0.135	12.53	2, 7
NGC6240	0.025	0.52	2.60	11.85	3
UGC5101	0.039	0.188	0.419	12.00	1, 2
Arp220	0.018	0.253	...	12.16	1
IRAS 05189	0.042	0.035	...	12.16	1
IRAS 08572	0.058	<0.012	...	12.14	1
IRAS 12112	0.073	0.517	0.569	12.33	1
IRAS 14348	0.083	0.254	...	12.35	1
IRAS 15250	0.055	0.023	...	12.05	1
IRAS 22491	0.077	0.594	0.671	12.19	1
NGC1569	$\sim$0	...	0.402	8.76	4
3C120	0.033	...	...	...	5
PG1612+261	0.131	...	...	...	5
PAH 1[a]	...	...	...	...	6
PAH 2[a]	...	...	...	...	6
PAH 3[a]	...	...	...	...	6
PAH 4[a]	...	...	...	...	6
PAH 5[a]	...	...	...	...	6

Notes.
[a] As explained in Smith et al. (2007b), those five templates are composite spectra computed in arbitrary units of νI_ν. We thus do not have corresponding redshift, luminosity or equivalent width.
References. (1) Armus et al. 2007; (2) Armus et al. 2004; (3) Armus et al. 2006; (4) Wu et al. 2006; (5) P. Ogle 2007, private communication; (6) Smith et al. 2007b; (7) Kim & Sanders 1998.

in Caputi et al. (2007) which was selected to have only sources with $S_{24} > 80$ μJy. Figure 13 shows our redshift distribution, and we compare it to that of Caputi et al. (2007).

4.2. Spectral Type

As presented above, the cross-correlation method provides spectroscopic redshifts along with an indication of the most similar spectral type. We have classified the sources in our sample by the best-fit template found for each. We divide the sources among four roughly defined populations: those distinguished by prominent aromatic emission features(14/45 sources), those characterized only by the presence of silicate absorption (4/45 sources), an intermediate population gathering mixed signatures from weak polycyclic aromatic hydrocarbon (PAH) and/or silicate absorption (8/45 sources), and those for which we could not find a redshift, and thus a spectral type (17/45 sources) either because of a very low S/N or because no features fall into the spectral band covered by this survey (14–21 μm or 20–35 μm). The absence of features in the spectrum can result from a high redshift ($z > 3.5$ in LL1 or $z > 2$ in LL2) or the intrinsic properties of a continuum-dominated source usually associated with a dominant AGN. Two sources for which we have been able to get a redshift are not part of any of the subsets described above. We will discuss these two in greater detail in the following section. It has been previously shown that H_2 lines can sometimes be detected even in low-resolution IRS spectroscopy (e.g., Armus et al. 2006, Dasyra et al. 2009). We do not, however, detect any reliable H_2 emission in our spectra. We show the complete spectral type statistics of the SUUSS sample for each field in Table 5.

A majority of the identified matches (14/28 sources) in our sample present some PAH emission features. The spectral ranges available cannot cover all the PAH bands at the same time, we refer to it as partial PAH emission. In spectra with limited MIR spectral coverage (in this case 14–21 μm or 20–35 μm), there is a degeneracy between a low S/N 7.7 μm PAH feature on the one hand and silicate absorption that creates a false "continuum bump" around 8 μm on the other. The easiest way to overcome this would be to ascertain the existence or absence of another PAH feature (e.g., 6.2 or 11.3 μm) not affected by the presence of SiO absorption. This is, however, almost impossible here due to the redshifts of our sources that tends to throw 6.2 or 11.3 μm rest-frame wavelength out of the observed spectral window.

Figure 14 shows spectra in rest frame (using $z_{\rm IRS}$ only) together with the best template. Templates have been normalized to the mean fluxes of our sources computed over the whole available spectral range. Provided a spectrum with a high enough

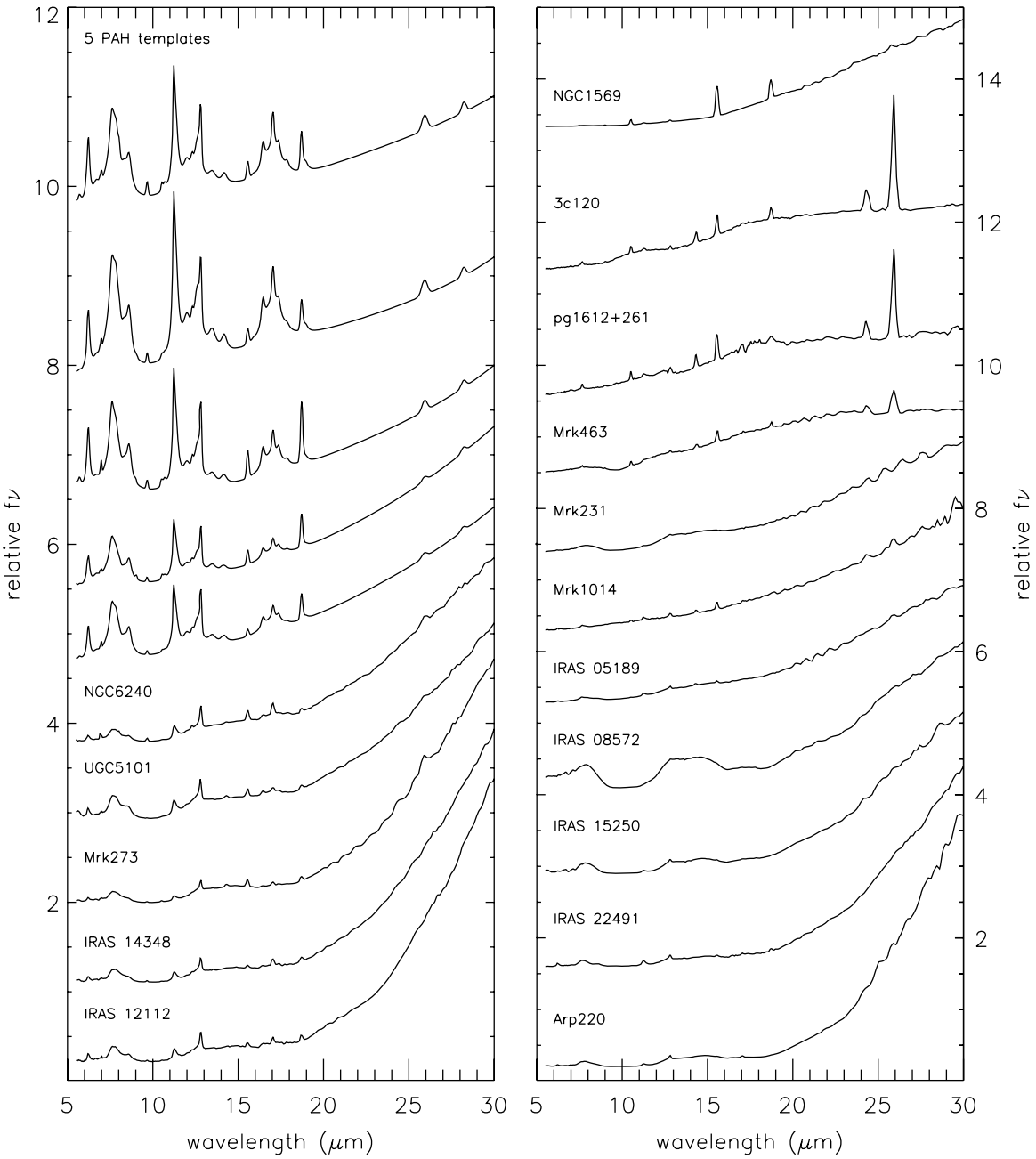

Figure 10. Full IRS low-resolution spectra (SL and LL modules) of all the templates used in the cross-correlation analysis. The five PAH templates are presented in Smith et al. (2007b). IRAS sources (05189, 08572, 12112, 14348, 15250, and 22491), Arp220, NGC6240, UGC5101, and Mrk 231, 273, 463, and 1014 are part of the IRAS bright sample. Their IRS MIR spectra are discussed in Armus et al (2006). The two QSO spectra (3c120 and PG1612+261) are from P. Ogle (2007, private communication). NGC1569 spectrum is presented in Wu et al. (2006).

S/N (empirically > 3) and enough dynamic range (measured as $\frac{\sigma_S}{\sigma_N} > 1$, cf. Equation (2) and Section 3.2), the effectiveness of the cross-correlation method will only be limited by the diversity of MIR spectral energy distribution (SED) shapes covered by our templates. These conditions lead to very good agreement as seen, for example, for sources SUUSS 20 or SUUSS 3 in Figure 14. Sharp cross-correlation peaks at the good redshift denote higher SED-feature "frequencies" (e.g., SUUSS 20, 30 or 25) such as 11.3 μm and 12.7 μm PAHs and/or atomic forbidden lines (e.g., [Ne III], [O IV]). On the other hand, wider cross-correlation maxima (usually ranging from high anti-correlation to high correlation) reveal a more diffuse identification based on the global shape of the spectrum ("lower signal frequencies") that we can see with low S/N 7.7 μm emission and SiO absorption (e.g., SUUSS 3, 41, or 42).

Analyzing results from Tables 4 and 5, we see that PAH templates from Smith et al. (2007b) provide most of the identifications (14 sources). These templates show PAH emission (6.2, 7.7 and/or 8.6 μm features, 12.8 μm emission line, etc), a "higher frequency" signal (compared to continuum and silicate absorption) that provides sharp cross-correlation peaks and thus more accurate and reliable redshift identification. A few other templates also match PAH emission features such as NGC6240 (two sources) or UGC5101 (one source) with differences being mainly on the continuum and the 11.3/7.7 ratio. Other identifications mostly rely on broad spectral behavior and

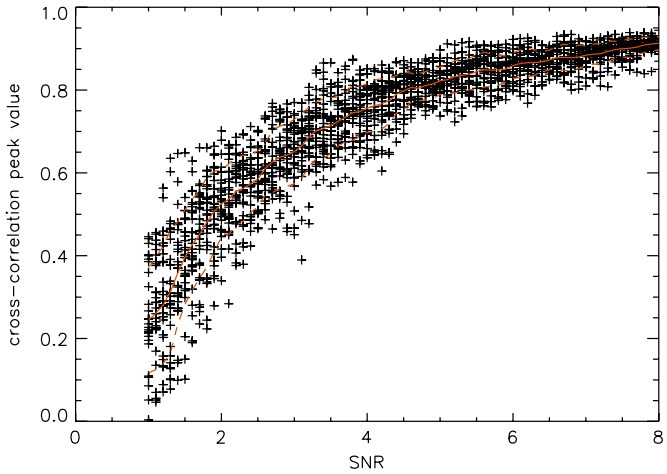

Figure 11. Value of a peak in a cross-correlation function as a function of the S/N in the data. We used a PAH template from Smith et al. (2007b) redshifted at $z = 1$. The modified template (with noise added) was cross-correlated with the original PAH template and the value of the peak (at $z = 1$ in the cross-correlation function) was tracked as a function of the noise. At each S/N, 30 realizations of the noise have been computed. The red curves show the mean $\pm 1\sigma$ of the distribution at each S/N value.

(A color version of this figure is available in the online journal.)

thus preferentially match templates such as Arp 220, Mrk231, Mrk463 or IRAS 15250 (six sources total). A few sources remain with in-between signal properties such as Mrk273 (two sources). Overall, the cross-correlation analysis provides strong characterization of MIR emission features in our sources, that we propose to use as a first-order diagnostic to distinguish between starburst and AGN as a power agent for these sources. For the featureless spectra, the cross-correlation method does not even yield a slope, and therefore generates limited information about the nature of the sources. We computed rest-frame composites for each group of sources with a redshift and similar spectral type. The increased S/N and spectral coverage are expected to allow us to determine additional global properties for those populations (cf. Section 5.1).

No spectral-type information could be extracted for the five sources for which we have an optical spectroscopic redshift but no IRS redshift. At least two of those have a MIR spectrum "polluted" by a spatially close and brighter source also present in our sample. While we have been able to separate spectra of confused sources in the previously described redshift identifications, in these two cases the "polluting" source was too strong in comparison and contributions could not be spatially or spectrally separated. For one of them (SUUSS 19) there is a hint of PAH emission (11.3 μm and 12.7 μm) in agreement with the existing optical spectroscopic redshift of the counterpart of $z = 1.013$.

4.3. Two Special Line-sources: [S IV] and [O IV] Lines

Among the detected sources, two (SUUSS 9 and 17) have only one prominent emission line each. In both cases, the redshift determination method had to be applied more carefully.

We observe SUUSS 9 at position 189.210 +62.2869 with a spectrum showing only one emission line at 32.40 μm (see Figure 15) with a total flux of $\sim 8 \times 10^{-19}$ W m^{-2}. A spurious origin for this feature was ruled out by several means, one of which was to build eight separate cubes (one from each AOR). The feature was found in five out of the eight cubes, which is consistent with the lower S/N when using only one-eighth of the data. The reliability of this source was further verified by inspection of its spatial profile. We integrated fluxes in a Hanning window centered on 32.4 μm and extracted the source PSF which matches that of brighter sources in our sample. We address the problem of assigning a redshift based on a single line by relying on our knowledge of typical MIR spectra of known sources, and by using surveys at other wavelengths in the same part of the sky for additional evidence. There are three GOODS sources (Chary 2007) sufficiently close to be considered as potential counterparts, as reported in NED (NASA/IPAC Extragalactic Database, 2008 December): GOODS J123650.87+621712.8 is 3.″4 away from our estimated position of SUSS9, and at a spectroscopic redshift of 2.133; GOODS J123650.22+621718.4 is 5.″5 away from SUSS9, and at $z = 0.51283$; GOODS J123649.44+621712.3 is 6.″7 away from SUSS9, and at a photometric redshift of 0.04.

Smith et al. (2007b) and Dale et al. (2006) have reported the detailed spectroscopic content of SINGS galaxies; similarly, Armus et al. (2007) reported on nearby ULIRGs. We will examine which of the most prominent lines seen in those systems might be associated with this one line, in view of the MIR spectral properties of those samples, and of the visible sources positionally associated with SUUSS9. We should clarify however that MIR spectra are still yielding many surprises, as in the case of radio galaxies (P. Ogle et al. 2009, in preparation), so that plausibility arguments presented here cannot yet be quantified as to their likelihood.

Molecular hydrogen is known to dominate the MIR spectra of certain objects, as in the case of Stephan's Quintet intergalactic shock (Appleton et al. 2006), or the Radio Galaxy system 3C 326 (Ogle et al. 2007). One possibility is that this could be the H_2 S(1) line at $z = 0.902$; one would then expect the S(2) line at 23.35 μm and the [Ne II] line at 24.36 μm, neither one of which is detected. In Stephan's Quintet, S(1) is the most luminous line, and each of [Ne II] and S(2) carries one-third or more of the luminosity in S(1); so their absence in SUUSS 9 is a significant argument against this possibility, as is the absence of any nearby visible sources at redshifts close to 0.9. Similarly, this could be the H_2 S(0) 28 μm line at $z = 0.148$, with the S(1) line expected at 19.55 μm, outside the survey spectral coverage. The lack of visible sources in the redshift vicinity of 0.148 argues against this possibility. Finally, if we assume this is the H_2 S(2) line at $z = 1.639$, then the S(3) would be expected at 25.5 μm, and it is not detected. The weak signal peaking around 16.97 μm (rest frame) is significantly removed from the expected wavelength. This non-detection is a strong argument given the typical weakness of the S(2) line, so we conclude this is an unlikely assignment.

The most prominent fine-structure lines that might be associated with the detection at 32.40 μm are [S IV] at $z = 2.083$, [Ne II] at $z = 1.529$, [Ne V] at $z = 1.262$, [Ne III] at $z = 1.083$, [S III] at $z = 0.731$, [O IV] at $z = 0.251$, or [Fe II] at $z = 0.247$. Among all these possibilities, we favor the [S IV] assignment, for two main reasons, one being the closest of the visible sources has a very similar redshift at $z = 2.133$, and the other being the existence of a similar MIR spectrum from the Local Universe, namely NGC1569 (Wu et al. 2006). The other potential assignments are less likely because the observed spectrum does not contain expected lines or aromatic features, and none corresponds to any of the redshifts of nearby sources. For instance, [Ne II] is quite unlikely to appear without aromatic features, and we would have detected the 11.3 μm band at 28.6 μm for $z = 1.529$. However, the radio galaxy 3C317 does display a

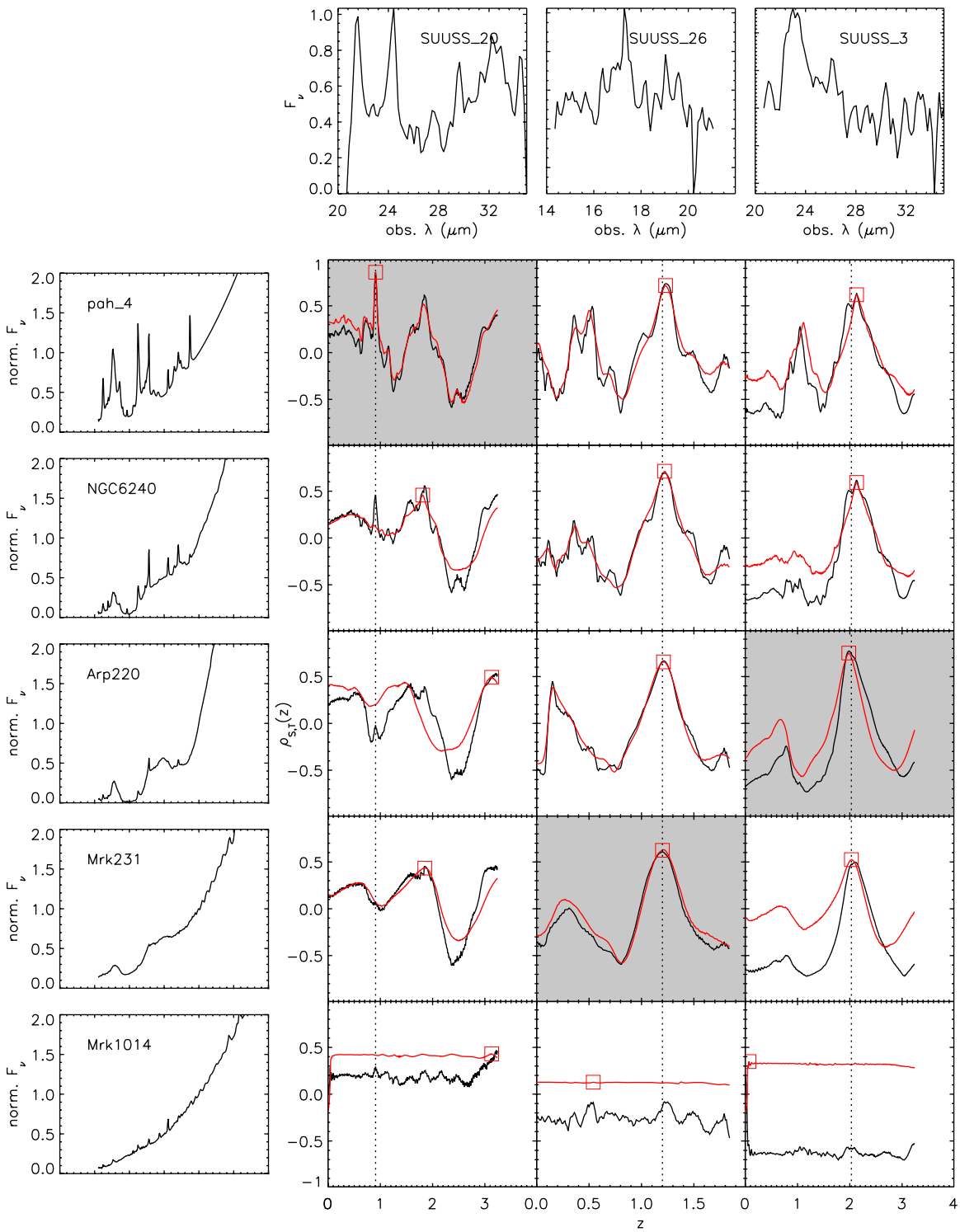

Figure 12. We represent the cross-correlation between three different spectra and five different templates with very diverse MIR spectral signatures. In each case, we show the cross-correlation function (black) and the auto-correlation function (red) for the best matching redshift (red square) with that specific template. The best candidate solution (redshift and template) for each source is shown as a gray-shaded plot.

(A color version of this figure is available in the online journal.)

high ratio of [Ne II] to aromatic features (P. Ogle et al. 2009, in preparation). Similarly, [Ne V] is generally much weaker than [Ne II], and the latter would have been detected at 26.7 μm for $z = 1.083$. [Ne III], on the other hand, can be much more luminous than [Ne II], thus appearing as the only line in a spectrum, but only in a small minority of cases. Dale et al. (2009) find that the [Ne III] flux exceeds twice the [Ne II] flux in less than 10% of the cases for a variety of SINGS objects. While it is possible that the line we detect is [Ne III], and that [Ne II] has escaped detection at 28.99 μm for $z = 1.262$, this redshift does not correspond to any objects in the field. The same argument applies to [S III], since [Ne II] would have been detected at 22.19 μm for $z = 0.731$, and it is rare for [S III] to exceed twice the flux of [Ne II]. The lines of [O IV] or [Fe II] near $z = 0.25$ are again

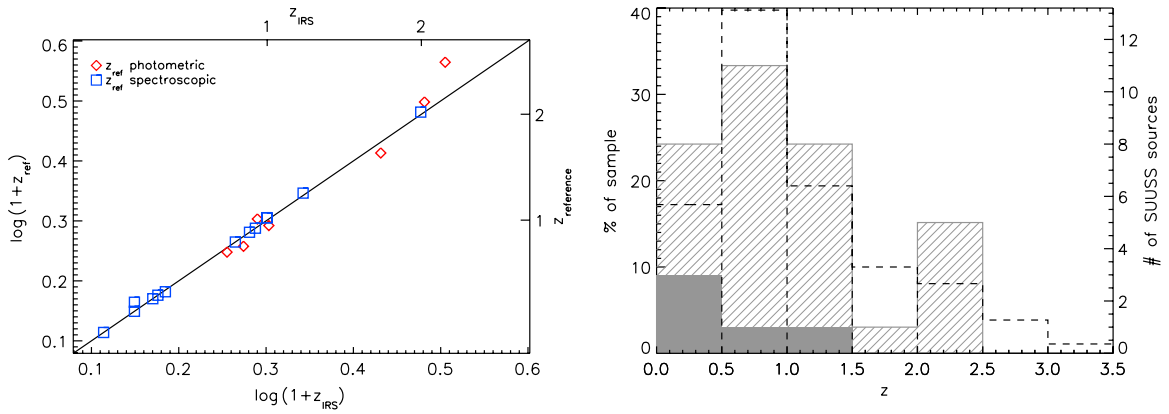

Figure 13. Left: IRS spectroscopic redshifts ($z_{\rm IRS}$) from our study against existing spectroscopic (TKRS, Wirth et al. 2004) and photometric (Caputi et al. 2007) redshifts ($z_{\rm ref}$). Right: redshift distributions. The dashed-gray histogram show the total redshift distribution for our sources ($z_{\rm IRS}$ supplemented with $z_{\rm ref}$ when $z$irs could not be obtained). The shaded histogram shows the sources for which we had only $z_{\rm ref}$. The dashed open histogram is Caputi et al.'s (2006) sample distribution. (A color version of this figure is available in the online journal.)

Table 4
Cross-correlation Analysis Results

ID	Field	$z_{\rm IRS}$	$z_{\rm ref}$[a]	$z_{\rm ref}$ Type[a]	Template	Spectral Type[b]
SUUSS 1	1	1.70	1.59	P	NGC6240	Mixed
SUUSS 2	1	0.50	0.50	S	PAH4	PAH
SUUSS 3	1	2.03	2.03	S	Arp220	Mixed
SUUSS 4	1	0.95	1.01	P	PAH4	PAH
SUUSS 8	1	0.65	...	...	PAH2	PAH
SUUSS 9	1	2.08	...	...	NGC1569	Line
SUUSS 14	1	2.20	2.67	P	Mrk273	Mixed
SUUSS 15	1	0.41	0.46	S	PAH3	PAH
SUUSS 17	1	0.30	0.30	S	pg1612+261	Line
SUUSS 18	1	2.04	...	...	IRAS 15250	SiO
SUUSS 20	1	0.91	0.91	S	PAH4	PAH
SUUSS 24	2	2.03	2.15	P	PAH5	PAH
SUUSS 25	2	0.84	0.84	S	PAH4	PAH
SUUSS 26	2	1.20	1.22	S	Mrk231	SiO
SUUSS 28	2	0.87	0.81	P	UGC5101	Mixed
SUUSS 29	2	0.94	0.94	S	PAH3	PAH
SUUSS 30	2	0.53	0.52	S	PAH5	PAH
SUUSS 32	2	0.20	...	...	PAH2	PAH
SUUSS 33	2	1.34	...	...	NGC6240	Mixed
SUUSS 34	2	1.21	...	...	Mrk231	SiO
SUUSS 36	2	0.61	...	...	PAH4	PAH
SUUSS 37	2	0.41	0.41	S	PAH2	PAH
SUUSS 38	2	1.23	...	...	Mrk463	SiO
SUUSS 39	2	0.48	0.48	S	PAH4	PAH
SUUSS 41	2	0.80	0.77	P	Arp220	Mixed
SUUSS 42	2	1.00	1.02	S	Mrk273	Mixed
SUUSS 44	2	1.00	1.02	S	IRAS 22491	Mixed
SUUSS 45	2	1.01	0.96	P	PAH1	PAH
SUUSS 12[c]	1	...	0.50	S	...	...
SUUSS 16[c]	1	...	0.46	S	...	...
SUUSS 19[c]	1	...	1.01	S	...	...
SUUSS 27[c]	2	...	0.30	S	...	...
SUUSS 31[c]	2	...	0.47	S	...	...

Notes.

[a] Spectroscopic (S) redshifts are from the Treasurey Keck Redshift Survey (Wirth et al. 2004) and photometric (P) redshifts are from Caputi et al. (2006).

[b] Sort the main spectral signature identified in the MIR spectra: PAH for strong aromatic features, SiO for silicate absorption, mixed for intermediate spectra, and line for the two line sources discussed in Section 4.3.

[c] Sources with no conclusive identification from the cross-correlation method but for which we had ancilliary redshifts (same reference).

Table 5
SUUSS Sample Statistics

Order	No. of Detections	Strong Aromatics	Mixed Signatures	Silicate Absorption	Strong Line	Featureless / Continuum
20–35 μm	20	5	3	1	2	9
14–20 μm	25	9	5	3	0	8

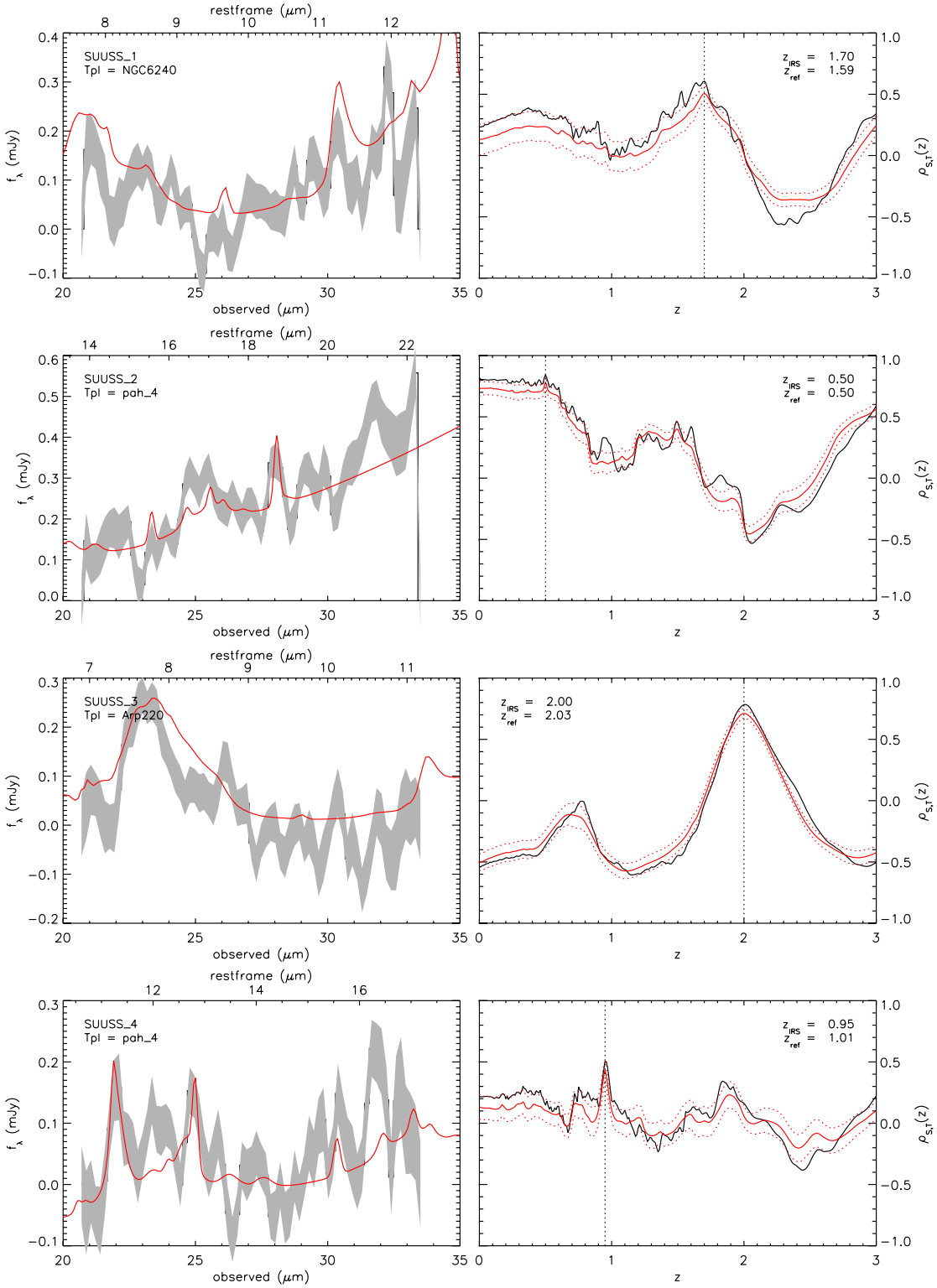

Figure 14. Left: our sources spectra (black) with best match template(red) overplotted. The template is scaled to the mean flux of the spectrum. Right: the related cross-correlation function (in black) and auto-correlation function (in red). The complete set of cross-correlation figures can be found in the online version of the journal.

(A color and an extended version of this figure are available in the online journal.)

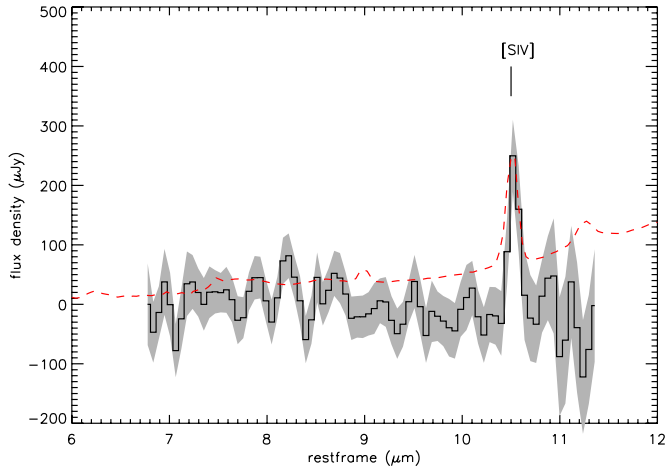

Figure 15. Spectrum of the [S IV] "line source" (SUUSS 9) in rest frame. 1σ deviation is shown as the gray shading. The cross-correlation gave us a redshift of $z = 2.08$ for this source. In dashed red, we show the spectrum of NGC1569 for which we obtained the best cross-correlation match. It is scaled to our source 10.5 μm rest-frame flux density.

(A color version of this figure is available in the online journal.)

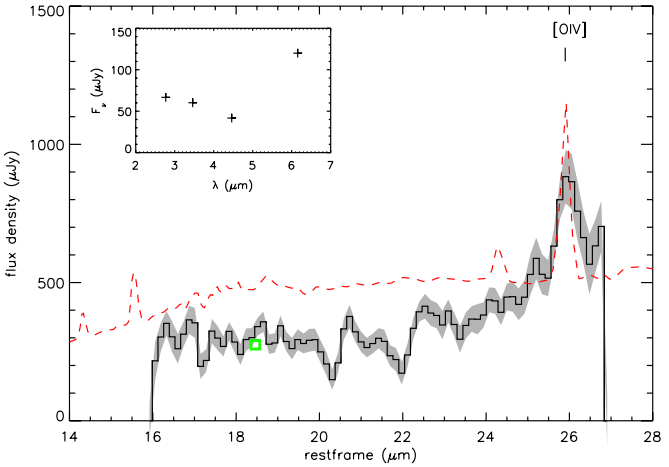

Figure 16. Spectrum of the [O IV] "line source" (SUUSS 17) in rest frame. 1σ deviation is shown as the gray shading. The green square is the MIPS 24 μm counterpart flux in rest frame. The cross-correlation, in agreement with ancillary data, gave us a redshift of $z = 0.3$ for this source. IRAC data points (inset) tend to agree with the presence of PAH emission at 6.2 μm. In dashed red, we plotted the spectrum of the QSO PG1612+261 for which we obtained the best cross-correlation match. It is scaled to our source 25.9 μm rest-frame flux density.

(A color version of this figure is available in the online journal.)

unlikely candidates, since the [S III] line is expected to be at least comparable in flux and detectable at 23.4 μm. The exception would be that [O IV] might exceed [S III] in AGN-dominated sources. However, the lack of a detectable continuum and the lack of a similar redshift in this vicinity are both arguments against this identification.

The close association of SUUSS9 with GOODS J123650.87+621712.8 both spatially and in redshift is suggestive of these being the same object, but not conclusive. It is just as likely that they are two neighboring sources rather than the same source. The redshift difference amounts to ∼15,000 km s^{-1} and corresponds to 1.7σ assuming that the uncertainty on the Reddy et al. (2006) redshift is sufficiently lower than ours. Moreover, interpreting SUUSS9 as a NGC 1569 analog implies that it is a Wolf–Rayet galaxy, whereas the GOODS source does not display the Wolf–Rayet characteristics in its optical spectrum (Brinchmann et al. 2008). Additional data will be required to clarify the relation between these two sources, which is beyond the scope of this paper. While we cannot attach a formal confidence level to this statement, we do propose that the interpretation of the SUUSS 9 line as [S IV] at $z \sim 2.1$ is the most plausible postulate, followed by the less likely interpretation as the H_2 S(0) line at $z = 0.15$. If SUUSS 9 is indeed detected in [S IV], then its [S IV] line luminosity would be 8.3×10^{35} W, whereas the dwarf galaxy NGC1569 emits 1.5×10^{31} W. While this is a dramatic difference, the [SIV] luminosity estimated for SUUSS9 is not extraordinary, in the sense that the quasar PG1612+261 has a comparable luminosity of 1.4×10^{35} W. The interpretation of the SUUSS 9 line as H_2 S(0) at $z = 0.15$ is less demanding energetically, since it requires scaling up the emission of the intergalactic shock in Stephan's Quintet by a factor of 11 only, to a line luminosity of 1.5×10^{33} W.

The second line sources (SUUSS 17) possess a relatively well determined MIR continuum of about 300 μJy ($> 6\sigma$) as can be seen in Figure 16. This source shows one very well defined emission line at $\lambda \sim 33.7$ μm (observed wavelength) with a total flux of $\sim 6 \times 10^{-19}$ W m^{-2}, and no other significant spectral feature over the LL1 wavelength range (20–35 μm). The two absorption-like features at 26 and 28.5 μm in the spectrum are unlikely to be real and are more likely originating from a combined effect of noise and confusion, as this source sit in a denser region of our survey with three surrounding sources as close as 15″. The line is well resolved by the IRS, with an estimated intrinsic full width at half-maximum equivalent to $\sim 4000 \pm 1400$ km s^{-1}. NED, consulted in 2008 December, reports three objects sufficiently close to be considered potential counterparts: GOODS J123658.45+621637.3 at $z = 0.2993$, and 1.″5 away, GOODS J123658.82+621638.1 at $z = 0.29863$, and 3.″2 away, and GOODS J123658.09+621639.4 at $z = 1.01734$ and 6.″2 away; all redshifts are from Wirth et al. (2004). The second of these is assigned a *Spitzer* 24 μm detection at 264 μJy, making it the most credible counterpart to SUUSS 17.

The cross-correlation analysis on this source yields several candidate solutions for different templates and does not allow us to secure a reliable redshift. However, using the $z = 0.3$ redshift as prior we find the best matching template to be the spectrum of pg1612+261 quasi-stellar object (QSO, Shi et al. 2007) with an IRS determined redshift of 0.3. This redshift implies that the strong emission line in the IRS (LL1) spectrum is either [O IV] (25.89 μm) or [Fe II] (25.99 μm). Moreover, at $z = 0.3$, the IRAC 8 μm band falls on top of the 6.2 μm feature and would be expected to cause an excess compared to the shorter wavelength IRAC bands. Such an excess is evident in the inset in Figure 16, and we tentatively interpret it as the presence of PAH emission. The difficulty with this interpretation, however, is that [O IV] is observed with < 1000 km s^{-1} width in known QSOs (e.g., Dasyra et al. 2008), and the line width observed for SUUSS 17, typical of broad-line region emission, is not expected for high-ionization species like [O IV]. It is also difficult to explain the large observed line width as resulting from the combination of [Fe II] and [O IV] emission, for the separation between the two lines is only 0.1 μm, or 900 km s^{-1}. One might invoke the possibility of a broadened [Fe II] rather than the [O IV], but one would then expect the 18.7 μm line of [S III] to be at least comparable, and typically several times stronger than [Fe II] (Dale et al. 2009). There is no evidence of the [S III] line in Figure 16, which argues against this possibility. The 17.94 μm line of [Fe II] is typically weaker than the 25.99 μm line, so we

would not expect it to appear. Another strong argument against SUUSS 17 displaying a broadened [Fe II] line is that this line is rarely seen as the dominant emission line from QSOs (e.g., Dasyra et al. 2008), and the lack of a strong [S III] line is more consistent with the observed line being [O IV] (e.g., Ogle et al. 2006).

Another possibility is that the 33.7 μm emission is an aromatic feature rather than a broadened line. We find this improbable, since other PAH features would be expected in the same spectral range: for example, if we assume that this emission feature is the 11.3 μm PAH (at $z = 1.98$) then emission at 7.7 μm rest frame should be observed at $\lambda = 23$ μm. While the overwhelming majority of sources follow this expectation, Leipski et al. (2009) show a clear counter-example in M84 (3C272.1), a FR-I radio galaxy with an IRS spectrum displaying the 11.3 μm feature but none of the features at 6 to 9 μm. However, given the strong evidence of an independent $z = 0.3$ determination for a spatially coincident source with the matching continuum flux density, we conclude that this possibility of $z = 1.98$ is much less likely than the $z = 0.3$ identification.

With the [O IV] at $z = 0.3$ identification, the large line width suggests the presence of a strong QSO. GOODS J123658.82+621638.1 is also detected with *Chandra* (Alexander et al. 2003). This is a soft X-ray-emitting source and falls in the "normal galaxy" category of Bauer et al. (2004) classification. In a more recent analysis by Georgakakis et al. (2007), the ratio of X-ray to infrared luminosity also places this source in the middle of the range for star-forming galaxies. Note also that prominent aromatics at 6.2 μm (Figure 16 inset) also argues for a strong star formation contribution to the luminosity of this source. This apparent contradiction with the measured line width in the spectrum may be the result of high dust attenuation affecting the X-ray luminosity, or simply due to multiple sources contributing to the IRS spectrum. The latter would not be surprising as the GOODS catalog contains two sources at $z \sim 0.3$ within 3.″2 of SUUSS 17. Here again, the additional work needed to resolve these ambiguities is beyond the scope of this paper.

5. DISCUSSION

This survey offers us a way to characterize the MIR population of galaxies in a small region of the sky down to very deep detection levels. While any survey samples the universe imperfectly, this survey avoids the bias of a narrow bandpass sampling complex SEDs. No bias is expected from the detection method used as it is only related to the integrated fluxes of the sources in the field and does not rely on any specific spectral feature detection.

We investigate the possibility that the analysis method presented here favors sources with specific types and redshifts in our field, potentially resulting in an a posteriori bias in the results. As explained in Section 3.1, the cross-correlation method is sensitive to the variance of the signal in the spectral window with respect to the variance of the noise. This means that the method gives better results when applied to spectra that show a significant structure such as strong emission lines, aromatic features or silicate absorption. Considering that the spectral window in our sample is limited to either 14–20 μm or 20–35 μm, this could lead to inhomogeneities or biases over redshift and type of sources for which the *cross-correlation* method was successful. If this effect is present, the only efficient way to remove it is to add multi-wavelength data (IRAC fluxes, near-IR and optical bands, etc.) to the spectra used in the cross-correlation algorithm thus lowering the probability of missing significant spectral information.

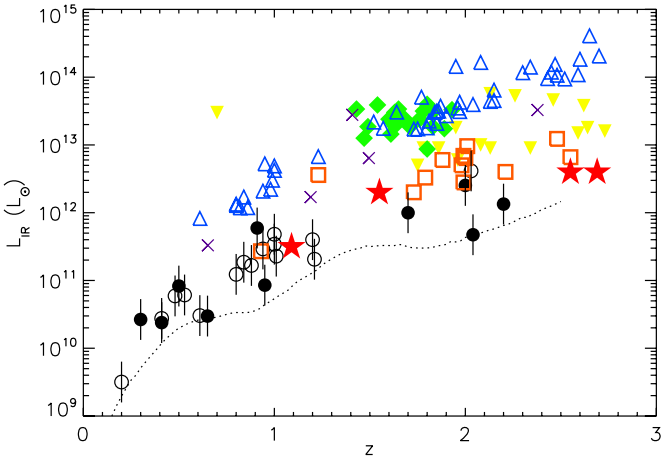

Figure 17. IR bolometric luminosities computed for our sample from MIPS 24 μm fluxes using a code provided by R. Chary implementing Chary & Elbaz (2001) and Dale & Helou (2002) models. Uncertainties are of 50%. We overplot IR luminosities of several other IRS surveys of high-redshifts galaxies. Filled dots are SUUSS sources from Field 1 and empty dots are SUUSS sources from Field 2, yellow filled triangles are 17 ULIRGS from the IRS GTO (Houck et al. 2005), blue open triangles are 47 ULIRGs from the XFLS (Yan et al. 2007), green diamonds are bump 2/3 sources from Farrah et al. (2008), orange open squares are 13 SMGs from the HDF-N SCUBA super-map (Pope et al. 2008), purple crosses are 5 SMGs from Menéndez-Delmestre et al. (2007), and red stars are from Teplitz et al. (2008). The dotted line is the luminosity limit of the SUUSS survey ($f_\nu(24\ \mu\text{m}) = 47\ \mu$Jy).

(A color version of this figure is available in the online journal.)

We discuss below the luminosities of the sources detected in this survey, then their MIR spectral character, and place them in the context of other surveys. We then contrast this unbiased spectral survey with single-band continuum surveys.

5.1. IR Luminosities and Spectral Types

Since we only have MIR data, we cannot compute accurate total IR luminosities. We could use the best template for each source, but some of the templates have no far-IR data, and 42% of the sources are not identified. We estimate IR bolometric luminosities from MIPS 24 μm flux measurements using a code made available online by R. Chary. The code selects the most appropriated SED from Chary & Elbaz (2001) and Dale & Helou (2002) models based on the 24 μm flux, fits the SEDs and computes the total 8–1000 μm IR luminosities, then averages them together. Figure 17 shows the source luminosities as a function of redshift. The luminosities range from $3.2 \times 10^9 L_\odot$ to $4.1 \times 10^{12} L_\odot$ with a mean of $5.2 \times 10^{11} L_\odot$. Even the four sources at $z \geqslant 2$ have an impressively low mean luminosity of $7.5 \times 10^{11} L_\odot$. When compared to existing IRS spectroscopic studies of high-redshift galaxies (Houck et al. 2005, Pope et al. 2006, Yan et al. 2007), our sample proves to be one of the deepest in this range of work (see Figure 17).

We selected all sources at $0.8 < z < 1.1$ (eight spectra) and at $1.7 < z < 2.2$ (four spectra, the "line-source" SUUSS 9 discussed in Section 4.3 was discarded from this sample) and computed corresponding composites (Figure 18). Each spectrum was scaled to its sample mean luminosity. The composite at $z \sim 1$ is dominated by aromatic features. We detect the 7.7, 8.6, and 11.3 emission features as well as the [Ne II] 12.8 μm line. We see generally agreement with the AGN-free starburst template from Brandl et al. (2006). Due to the lack of spectral

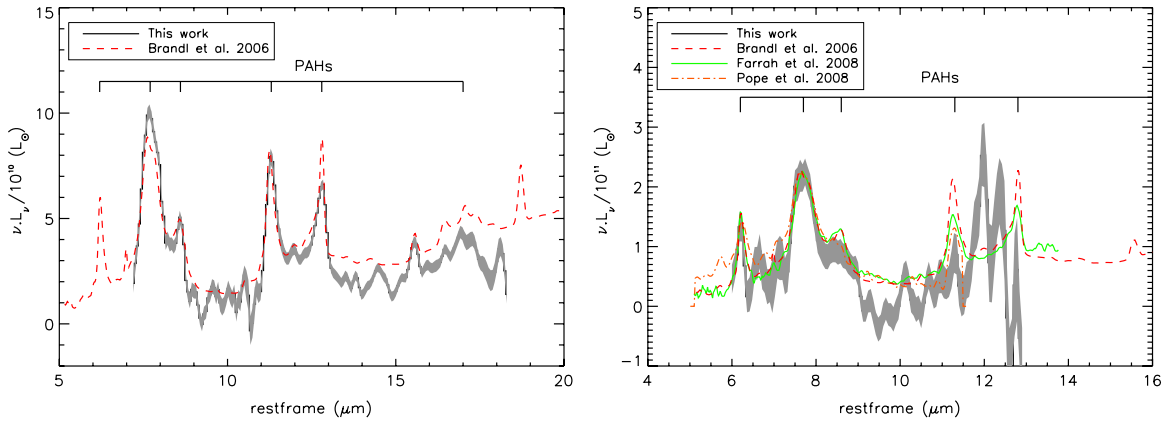

Figure 18. Left: composite spectrum at $z = 1 \pm 0.2$. Right: composite spectrum at $z \sim 2$. In gray shading we plot the 1σ dispersion for each composite. In dashed red, we overplot the "starburst average spectrum" from Brandl et al. (2006) scaled to our composites 8.6 μm and 7.7 μm luminosities at $z = 1$ and $z \sim 2$ respectively. We also plot in green average spectrum from Farrah et al. (2008) and in orange $z \sim 2$ average spectrum from Pope et al. (2008). Both composites are dominated by PAH emission at 7.7 μm and agree very well with the starburst template. The 11.3 μm PAH detection in the $z \sim 2$ composite is not clear. This part of the composite ($\lambda > 10$ μm) is particularly affected by the noise.

(A color version of this figure is available in the online journal.)

coverage in this $z \sim 1$ sample, we have no data at λ greater than 17 μm.

In the composite at $z \sim 2$, we can clearly see 6.2, 7.7, and 8.6 μm PAHs. In comparison to $z \sim 1$, this sample of sources is half an order of magnitude more luminous. We also cannot confirm or rule out the presence of any emission at 11.3 μm, although this feature is very often detected across the entire sample of this study. This may be due to the small number of sources entering the $z \sim 2$ composite together with increased noise at this rest-frame wavelength. The shape and relative strengths of the 7.7 and 8.6 μm features are, however, conserved between $z \sim 1$ and $z \sim 2$. The four sources that enter this composite all show a clear stellar bump in the IRAC channels which is expected for starburst galaxies between $z = 1.7$ (bump 2) and $z = 2.2$ ($\sim$ bump 3). As seen by Farrah et al. (2008) in their sample of 32 high-redshift ultraluminous infrared galaxies selected as bump two sources (mainly), composite spectra of such sources are best described by a starburst component, namely the template produced by Brandl et al. (2006). Little silicate absorption is seen in the Farrah et al. sample and none is seen in our composites either. The same observation is made on the population of submillimeter-selected high-redshift infrared galaxies presented in Menéndez-Delmestre et al. (2007) and Pope et al. (2008) where a starburst scenario (Brandl et al. 2006 template or M82) with low-AGN contribution better fits the composite spectra. Previous work by Houck et al. (2005) or Sajina et al. (2007) find prominent and/or non-negligible SiO absorption in their sources (55% and 33% of the samples respectively). Our $z \sim 2$ composite is surprisingly quite similar to the composite of $z \sim 2$ sources presented in Sajina et al. (2007) with the exception of the slight SiO absorption. Overall, we observe MIR composite spectra generally similar to those derived from other samples of high-redshift ($1 < z < 2.5$) infrared galaxies with very different selection criteria and bolometric luminosities, and generally favoring a starburst character.

5.2. Characterizing the Population (AGN Versus Starburst ?)

Table 5 summarizes the statistics of spectral types assigned for objects detected in this survey. We assigned each spectral template used to one of the three classes, namely strong aromatics, silicate absorption, and mixed signatures. The counts of objects falling in each category are shown in Columns 3, 5, and 4, respectively; Column 7 accounts for sources which could not be matched using the spectral correlation method. The two sources discussed in Section 4.3 were gathered in a fourth class (Column 6). Among the sources with accepted matches, about half (14 out of 28) are dominated by the aromatic features and another third (eight out of 28) have a mixed character. About 15% (four out of 26) have substantial silicate absorption, indicative of high optical depth, against a dominant continuum suggesting a major AGN contribution. Out of the total sample of 45 sources, 17 could not be matched to any templates in our library. This might be due to their being dominated by a featureless continuum, or to their low S/N. If the former is the dominant cause, then these 17 might be primarily AGN-dominated sources, and the statistics among matched spectra are biased toward starburst signatures.

In order to rule out a bias in favor of starburst galaxies among matched spectra, we used additional diagnostics based on IRAC and MIPS color–color plots (Figure 19). They can be used to separate AGN-dominated sources up to $z \sim 2$ (e.g., Donley et al. 2008). According to these diagnostics, no clear AGN-dominated system is detected in our total sample of 45 sources, which is consistent with the redshift and spectral-type determination among sources matching templates. The sources in our sample therefore seem to be mostly dominated by star formation, and this result is not a bias due to the spectral matching technique.

We have also used X-ray data for this region from the *Chandra* Deep Field North 2Ms catalog (Alexander et al. 2003) to look for X-ray counterparts to our sources. We found four matches inside a 3 arcsec matching radius. Following the classification proposed by Bauer et al. (2004), two of them are potential X-ray obscured AGNs (SUUSS 31 and 41), and one is a starburst galaxy clearly identified as such with our data set (SUUSS 20). The last X-ray counterpart is the [O IV] line source previously described in Section 4.3. Three additional counterparts were identified using the supplementary catalog; these are sources that were not detected with a high enough significance to be included in the main 2Ms X-ray catalog. They are fainter sources but have an optical counterpart which makes them highly likely to be real X-ray sources and potential candidates for faint AGNs. One of them presents PAH emission with possible silicate absorption, one is clearly continuum dominated (with 17 μm PAH emission

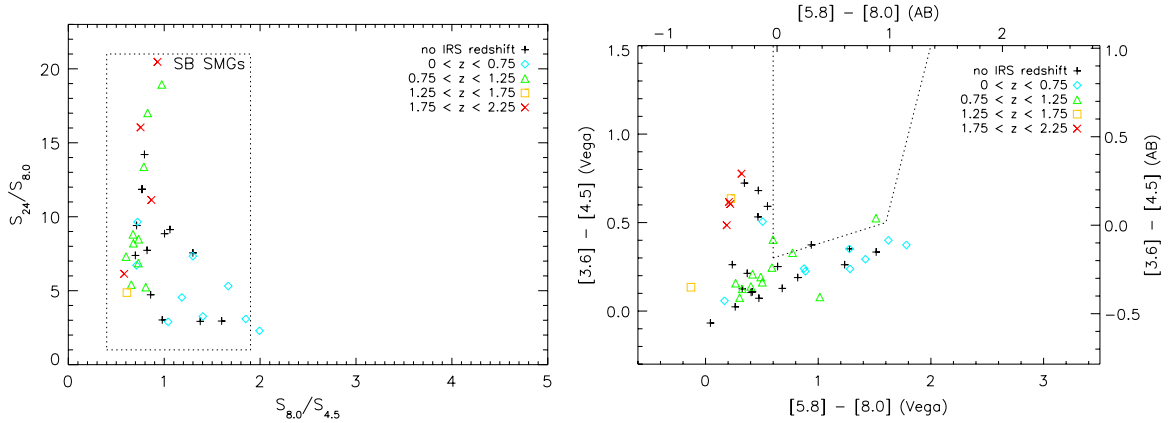

Figure 19. *Spitzer* color–color diagram characterization of the IRS Ultradeep survey sample of galaxies. Left: AGN diagnostic proposed by Pope et al. (2008) determined from a sample of 13 SMGs from z ∼ 1 to 2.5 (see also Ivison et al. 2004). Right: AGN diagnostic using IRAC colors, explained in Stern et al. (2005). The Broad-Line AGN selection criteria are represented by the dotted line. The lower and left-hand axes are scaled to Vega magnitudes, whereas the top and right-hand axes refer to AB magnitudes.

(A color version of this figure is available in the online journal.)

detected), and the last one has deeper silicate absorption which give us two other possible AGN identifications. Tentatively, we estimate an AGN fraction of 4 out of 45 (9%) of our sample, based on X-ray detections. Given the sample size, this is consistent with the spectral typing results summarized above.

The IRS GTO observations of Houck et al. (2005) unveiled a population of sources dominated by strongly obscured (SiO absorption) AGNs, some presenting PAH signatures even though faint. The Yan et al. (2007) sample of 52 ULIRGs has more diverse properties with roughly a third of the sources presenting strong PAHs, another third showing strong silicate absorption, and the rest being continuum sources sometimes with weak features. These sources show large AGN contributions (80% of the sample has some level of AGN continuum signature) with a significant fraction of sources having a starburst signature as well (Yan et al. 2007; Sajina et al. 2007). These two samples have very different AGN fractions and SiO absorption depths in comparison to our sample. However, these samples also derive from quite different selection criteria and flux densities. We will address below the relation between the AGN fraction differences and the sample selection.

Previous studies have shown submillimeter galaxies at high redshifts to be dominated by starburst emission (Egami et al. 2004; Ivison et al. 2004; Pope et al. 2006). Thus, a comparison of our sample with the Pope et al. (2008) sample may be useful. As we already discussed, both samples have very similar composite spectra at $1 < z < 2.5$. While X-ray classification tends to show the presence of AGNs in about 40% of those sources, star formation is found to account for more than half the bolometric luminosity. An interesting way of computing MIR photometric redshifts was proposed in Pope et al. (2006) using all four IRAC bands and MIPS 24 μm fluxes to give an estimate of the redshift. This method assumes a fairly constant SED shape across the sample and thus is spectral-type dependent. We produced a similar formula for our sample by fitting to the redshift obtained with the cross-correlation method:

$$z_{\rm IR} = a + b \cdot \log(\mathrm{S}_{3.6}) + \mathrm{c} \cdot \log(\mathrm{S}_{5.8}) + d \cdot \log(\mathrm{S}_{8.0}) + \mathrm{e} \cdot \log(\mathrm{S}_{24}), \quad (5)$$

where the fitting parameters values are 1.7, −2.6, 3.3, −1.0, and 0.1 for a, b, c, d, and e, respectively. We find the deviation of the redshift statistic to be of $\sigma\,(\Delta z/(1+z)) = 0.22$ which is rather large compared to the dispersion of $\sigma\,(\Delta z/(1+z)) = 0.07$ found in Pope et al. (2006), perhaps explained by the fact that our SEDs that enter the fit have a wide variety of spectral types. However, no selection could be found that, when applied to our sample, reduced the dispersion. It is, therefore, very likely that there is a larger diversity of SEDs in our sample compared to the 13 SMGs studied by Pope et al. (2008), even though both have very similar average MIR spectra.

5.3. Unbiased Spectral Surveys: A Different Probe

While our survey covers a small solid angle and the data are collected over two separate spectral windows, it still yields a somewhat different perspective on the MIR universe at $z \leqslant 2$ and illustrates some of the distinguishing characteristics of wide-band spectral surveys. The basic statistics, summarized in Table 5, point to a relative paucity of AGN signature among SUUSS sources compared to other deep spectral surveys such as Weedman et al. (2006) or Yan et al. (2007). The same lack of AGN signatures is observed in IRAC color–color diagnostic plots of SUUSS sources, so it is very unlikely to reflect a bias introduced by the spectral correlation technique. This difference is partly due to additional selection criteria imposed on the other surveys, partly due to the fainter flux densities and luminosities of the SUUSS sample, but probably also in part due to the reduced selectivity of an unbiased spectral survey.

The Yan et al. and Weedman et al. samples were both selected for high 24 μm/R ratios, with an additional selection for high 24/8 μm ratios by Yan et al. These choices were aimed at biasing toward high redshifts and luminosities, and indeed they achieve that as can be seen in Figure 17. Aromatic features dominate the spectra of no more than a third of those samples. The selection for high 24 μm/8 μm or 24 μm/R favors high obscuration, which is mildly anti-correlated with aromatic signatures (Sajina et al. 2007), and might therefore reduce the incidence of aromatic features in those samples.

On the other hand, the SUUSS sample has a median $f_\nu(24\ \mu\mathrm{m}) \sim 100\ \mu$Jy, whereas the other samples are brighter by one order of magnitude for Yan et al., and almost three orders of magnitude for Weedman et al. The lower fluxes lead to lower luminosities, and would generally favor star formation powered systems over AGNs, translating into a preponderance

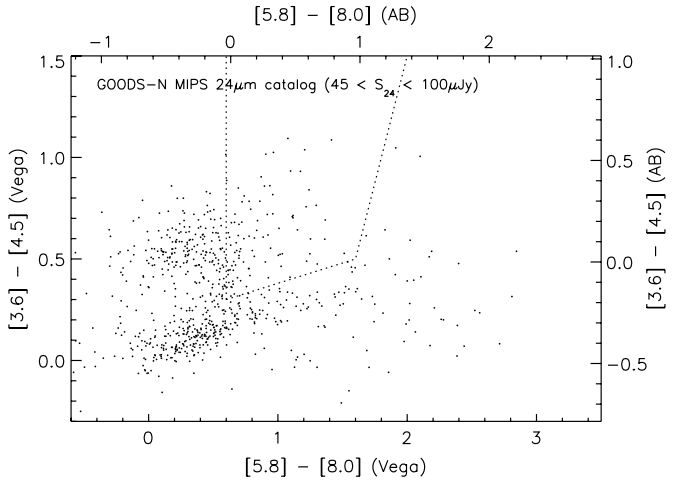

Figure 20. IRAC color–color diagram for all GOODS-N sources with identified MIPS 24 μm flux such as 45 μJy $< f_\nu(24\ \mu\text{m}) <$ 100 μJy. 823 sources fall into this category and only 93 of them enter the AGN region of the diagram i.e., 11% of the sample. This low ratio indicates the importance of the detection limit on the ratio of AGN-dominated system over starburst-dominated system found in flux limited surveys.

of aromatic-feature-rich spectra (Papovich et al 2007). Given the evidence at hand, we favor this interpretation as the dominant factor in determining the spectral characteristics of this sample.

The IRAC colors of the SUUSS sample also point to a lack of objects residing in the AGN-dominated part of that diagnostic plot (Figure 19). The same diagnostic is used over all the GOODS-N sources with a MIPS 24 μm flux in between 45 and 100 μJy (Figure 20). Out of the 823 sources that fall into this category only 93 (11%) are found in the AGN-dominated part of the diagram. The effect observed in the SUUSS sample is thus most probably due to its lower mean luminosity, which results from the sensitivity achieved but also from the choice of a particularly dark survey field.

Other factors may affect the character of SUUSS sources. One possibility is that spectra with more features, i.e., larger σ_S, are easier to pick out in a spectrally dispersed survey than in a traditional single-band survey, since a feature would have to coincide with the survey filter to generate a signal. Thus single-band surveys would favor continuum-dominated sources at all redshifts, bias against those whose absorption features fall into the band and bias for sources whose emission features fall into the band. This may explain the preponderance of an AGN in 24 μm-selected samples (e.g., Daddi et al 2007). Figure 7, right-hand panel illustrates the lack of selectivity in this survey, as it shows most sources peak away from 24 μm, and indeed have higher fluxes where detected than at 24 μm.

The 24 μm survey obviously missed the single-line source SUUSS 9, since the line fell outside the 24 μm band. Since we found one such source in the whole survey, the incidence of such sources in general must be of the order of 2%–4%, depending on what we assume for the efficiency of our search. Since this source does not have a 24 μm counterpart, we can only assign an upper limit to its luminosity as defined in Figure 17. That upper limit is roughly $5 \times 10^{11} L_\odot$, based on the 24 μm detection limit.

The wavelength coverage in this survey was either 14–21 μm or 20–35 μm. This limited spectral coverage has contributed to the difficulty of identifying a spectral match for more than a third of the detections, and to the difficulty of identifying the single line detected in SUUSS 9. Future IR spectral surveys would be more productive if they covered at least a full octave in wavelength.

6. CONCLUSION

We have obtained IRS spectra for 45 sources of very faint IR galaxies and determined redshifts for $\sim$ 60% (28/45 sources) of them using a specifically designed cross-correlation method. We covered a domain of IR luminosities from about $7 \times 10^{10} L_\odot$ at $z = 0.5$ to about $10^{12} L_\odot$ at $z \sim 2.0$ poorly covered by IRS spectroscopy so far. At least 47% of our sample show starburst activity as PAH signatures (up to 21/45 sources) and 31% (14/45 sources) prove to be starburst dominated. The rest of the redshift identifications rests on silicate absorption feature (11% or 5/45 sources). We tentatively identify only 9% of our sample (4/45 sources) as AGN candidates. This small fraction of the AGN in comparison to previous IRS spectroscopic surveys of high-redshift galaxies is likely to originate from the fainter luminosities reached here. We find two unusual sources with only one prominent emission line detected over the spectral range covered. One of them presents a strong [O IV] line (25.9 μm rest frame) at $z = 0.3$ on top of a significant continuum, while the other shows the [S IV] line (10.5 μm rest frame) at $z = 2.08$ on a very weak continuum dominated by instrumental noise.

We thank Aaron Stephen for help with the X-ray data. This work is based on observation obtained with the *Spitzer Space Telescope*, which is operated by the Jet Propulsion Laboratory, California Institute of Technology, under NASA contract 1407. Support for this work was provided by NASA through an award issued by JPL/Caltech, as well as the French National Agency for Research under programs ANR-06-BLAN-0170 and ANR-05-BLAN-0289-02. This research has made use of the NASA/IPAC Extragalactic Database which is operated by JPL/Caltech, under contract with NASA.

Facilities: Spitzer (IRS)

REFERENCES

Alexander, D. M., et al. 2003, AJ, 126, 539
Appleton, P. N., et al. 2006, ApJ, 639, L51
Armus, L., et al. 2004, ApJS, 154, 178
Armus, L., et al. 2006, ApJ, 640, 204
Armus, L., et al. 2007, ApJ, 656, 148
Bauer, F. E., et al. 2004, AJ, 128, 2048
Brandl, B. R., et al. 2006, ApJ, 653, 1129
Brinchmann, J., Kunth, D., & Durret, F. 2008, A&A, 485, 657
Caputi, K. I., et al. 2006, ApJ, 637, 727
Caputi, K. I., et al. 2007, ApJ, 660, 97
Chary, R., & Elbaz, D. 2001, ApJ, 556, 562
Chary, R.-R. 2007, in ASP Conf. Ser. 380, Deepest Astronomical Surveys, ed. J. Afonso et al. (San Francisco, CA: ASP), 375
Dale, D. A., & Helou, G. 2002, ApJ, 576, 159
Dale, D. A., et al. 2006, ApJ, 646, 161
Dale, D. A., et al. 2009, ApJ, 693, 1821
Dasyra, K. M., et al. 2008, ApJ, 674, L9
Dasyra, K. M., et al. 2009, ApJ, 701, 1123
Dickinson, M., Giavalisco, M., & The Goods Team 2003, in The Mass of Galaxies at Low and High Redshift, ed. R. Bender & A. Renzini (Berlin: Springer-Verlag), 324
Dole, H., et al. 2001, A&A, 372, 364
Dole, H., et al. 2004, ApJS, 154, 93
Donley, J. L., Rieke, G. H., Perez-Gonzalez, P. G., & Barro, G. 2008, ApJ, 687, 111
Egami, E., et al. 2004, ApJS, 154, 130
Elbaz, D., et al. 1999, A&A, 351, L37
Farrah, D., et al. 2008, ApJ, 677, 957

Georgakakis, A., Rowan-Robinson, M., Babbedge, T. S. R., & Georgantopoulos, I. 2007, MNRAS, 377, 203
Helou, G., & Beichman, C. A. 1990, in Liege Int. Astrophys. Colloq. 29, From Ground-Based to Space-Borne Sub-mm Astronomy, ed. B. Kaldeich (Princeton, NJ: Princeton Univ. Press), 117
Houck, J. R., Weedman, D. W., Le Floc'h, E., & Hao, L. 2007, ApJ, 671, 323
Houck, J. R., et al. 2004, ApJS, 154, 18
Houck, J. R., et al. 2005, ApJ, 622, L105
Ivison, R. J., et al. 2004, ApJS, 154, 124
Kim, D.-C., & Sanders, D. B. 1998, ApJS, 119, 41
Lagache, G., Dole, H., & Puget, J.-L. 2003, MNRAS, 338, 555
Le Floc'h, E., et al. 2004, ApJS, 154, 170
Le Floc'h, E., et al. 2005, ApJ, 632, 169
Leipski, et al. 2009, submitted
Lu, N., et al. 2003, ApJ, 588, 199
Menéndez-Delmestre, K., et al. 2007, ApJ, 655, L65
Narron, R., Ogle, P., & Laher, R. R. 2007, in ASP Conf. Ser. 376, Astronomical Data Analysis Software and Systems XVI, ed. R. A. Shaw, F. Hill, & D. J. Bell (San Francisco, CA: ASP), 437
Ogle, P., Antonucci, R., Appleton, P. N., & Whysong, D. 2007, ApJ, 668, 699
Ogle, P., Whysong, D., & Antonucci, R. 2006, ApJ, 647, 161
Oliver, S., et al. 2000, MNRAS, 316, 749
Papovich, C., et al. 2007, ApJ, 668, 45
Pope, A., et al. 2006, MNRAS, 370, 1185
Pope, A., et al. 2008, ApJ, 675, 1171
Reddy, N. A., Steidel, C. C., Erb, D. K., Shapley, A. E., & Pettini, M. 2006, ApJ, 653, 1004
Rieke, G. H., et al. 2004, ApJS, 154, 25
Rowan-Robinson, M. 2001, ApJ, 549, 745
Rowan-Robinson, M., et al. 2004, MNRAS, 351, 1290
Sajina, A., et al. 2007, ApJ, 664, 713
Shi, Y., et al. 2007, ApJ, 669, 841
Smith, J. D. T., et al. 2007a, PASP, 119, 1133
Smith, J. D. T., et al. 2007b, ApJ, 656, 770
Soifer, B. T., Helou, G., & Werner, M. 2008, ARA&A, 46, 201
Stern, D., et al. 2005, ApJ, 631, 163
Teplitz, H. I., et al. 2007, ApJ, 659, 941
Weedman, D. W., et al. 2006, ApJ, 651, 101
Werner, M. W., Gallagher, D. B., & Irace, W. R. 2004, Adv. Space Res., 34, 600
Wirth, G. D., et al. 2004, AJ, 127, 3121
Wu, Y., et al. 2006, ApJ, 639, 157
Yan, L., et al. 2004, ApJS, 154, 75
Yan, L., et al. 2007, ApJ, 658, 778